



DISSIPATIVE PARTICLE DYNAMICS SIMULATION OF MECHANICAL
PROPERTIES OF SINGLE-WALLED CARBON NANOTUBE-
POLYISOPRENE COMPOSITES

BY

MR RANGSIMAN KETKAEW

A THESIS SUBMITTED IN PARTIAL FULFILLMENT OF THE REQUIREMENTS
FOR THE DEGREE OF MASTER OF SCIENCE (CHEMISTRY)

DEPARTMENT OF CHEMISTRY
FACULTY OF SCIENCE AND TECHNOLOGY
THAMMASAT UNIVERSITY

ACADEMIC YEAR 2018

COPYRIGHT OF THAMMASAT UNIVERSITY

DISSIPATIVE PARTICLE DYNAMICS SIMULATION OF MECHANICAL
PROPERTIES OF SINGLE-WALLED CARBON NANOTUBE-
POLYISOPRENE COMPOSITES

BY

MR RANGSIMAN KETKAEW



A THESIS SUBMITTED IN PARTIAL FULFILLMENT OF THE REQUIREMENTS
FOR THE DEGREE OF MASTER OF SCIENCE (CHEMISTRY)

DEPARTMENT OF CHEMISTRY
FACULTY OF SCIENCE AND TECHNOLOGY
THAMMASAT UNIVERSITY

ACADEMIC YEAR 2018

COPYRIGHT OF THAMMASAT UNIVERSITY

THAMMASAT UNIVERSITY
FACULTY OF SCIENCE AND TECHNOLOGY

THESIS

BY

MR RANGSIMAN KETKAEW

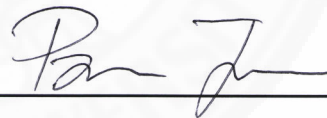
ENTITLED

DISSIPATIVE PARTICLE DYNAMICS SIMULATION OF MECHANICAL PROPERTIES OF
SINGLE-WALLED CARBON NANOTUBE-POLYISOPRENE COMPOSITES

was approved as partial fulfillment of the requirements for
the degree of master of science (chemistry)

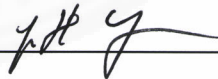
on December 11st, 2018

Chairman



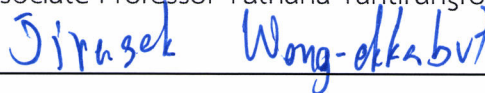
(Panichakorn Jaiyong, Ph.D.)

Member and Advisor



(Associate Professor Yuthana Tantirungrotechai, Ph.D.)

Member



(Associate Professor Jirasak Wong-ekabut, Ph.D.)

Member



(Siriporn P. Naprasertkul, Ph.D.)

Dean



(Associate Professor Somchai Chakatrakarn, Ph.D.)

Thesis Title	DISSIPATIVE PARTICLE DYNAMICS SIMULATION OF MECHANICAL PROPERTIES OF SINGLE- WALLED CARBON NANOTUBE-POLYISOPRENE COMPOSITES
Author	Mr. Rangsiman Ketkaew
Degree	Degree of Master of Science (Chemistry)
Department/Faculty/University	Department of Chemistry Faculty of Science and Technology Thammasat University
Thesis Advisor	Assoc. Prof. Yuthana Tantirungrotechai, Ph.D.
Academic Year	2018

ABSTRACT

Raw natural rubber (NR) or polyisoprene (PI) is low mechanical strength material such that can be improved by reinforcement filler. Previous experimental studies on the mechanical properties of NR have reported that single-walled carbon nanotubes (SWCNTs) enhance the strength of PI composite noticeably. This thesis aims to study the role of SWCNT in morphology and mechanical properties of cross-linked PI nanocomposites using dissipative particle dynamics (DPD) simulation. Polyisoprene composited with SWCNT (2%, 4%, 6%, and 8%) were simulated by DPD. Although the polymer dynamics can be described by the coarse-grained DPD simulation, the polymer chain crossing (topology violation) can be found during simulation. The modified segmental repulsive potential (mSRP) is introduced in conjunction with DPD to simulate the PI entanglement. The DPD and DPD/mSRP models were used to predict the stress-strain curve and compared to experimental test. The Young's modulus was computed as a function of % mixture. Self-aggregation of SWCNT at high concentration on morphology of PI was investigated. Analysis of structural and dynamical functions such as radial distribution function, were used to monitor the change of structural behavior during deformation. An increase of mechanical strength

of PI nanocomposites was attributed to the self-aggregation and movement direction of SWCNT. We also reparameterized the repulsive interaction parameter of PI to reproduce the experimental value. Our suitable computational protocol and suggested parameter are essential for DPD simulation. Knowledge of mechanical properties is useful for long-term study of an entangled PI composites with reinforcement filler.

Keywords: Natural rubber, Mechanical properties, DPD, entangled polymer



ACKNOWLEDGEMENTS

I thank Professor Yuthana Tantirungrotechai for five years of support, advice, and knowledge. I will forever be grateful. I acknowledge the moral support provided by my family and the patience they have shown. I thank all past and current members of the computational chemistry research unit for their help. I acknowledge Professor Jen-Shiang K. Yu, NCTU, Taiwan for his support and hospitality throughout my internship in Taiwan. Finally, I thank UBE Chemicals (Asia) Public Co., Ltd., Rayong, Thailand for inspiring this work and providing financial support.

Mr. Rangsiman Ketkaew



(4)

TABLE OF CONTENTS

	Page
ABSTRACT	(1)
ACKNOWLEDGEMENTS	(3)
TABLE OF CONTENTS	(4)
LIST OF TABLES	(7)
LIST OF FIGURES	(8)
LIST OF ABBREVIATIONS	(11)
CHAPTER 1 INTRODUCTION	1
1.1 Statement of Problems	1
1.2 Objectives	6
1.3 Thesis organization	7
CHAPTER 2 REVIEW OF LITERATURE	8
2.1 Theoretical background	8
2.1.1 Dissipative particle dynamics	8
2.1.2 Segmental repulsive potential	11
2.2 Young's modulus test	13
2.2.1 Simulation of modulus	14
2.3 Literature review	15
CHAPTER 3 RESEARCH METHODOLOGY	21

3.1 DPD parameterization	21
3.2 DPD bead modeling	23
3.2.1 Modeling of PI	23
3.2.2 Modeling of SWCNT	24
3.2.3 Modeling of cross-link	24
3.3 Simulation protocol	26
3.3.1 Molecular configuration setup	26
3.3.2 Dynamics simulation	27
3.4 Post-simulation analysis	29
3.4.1 Molecular visualization	29
3.4.2 Mean-squared displacement	29
3.4.3 Root mean-squared end-to-end distance	29
3.4.4 Radial distribution function	30
3.4.5 Orientational order parameter	30
3.4.6 Cluster analysis	31
CHAPTER 4 RESULTS AND DISCUSSION	32
4.1 Entanglement property	32
4.1.1 Effect of cross-links	32
4.1.2 Effect of self-avoiding model	34
4.2 Thermodynamics and structural stabilities	35
4.2.1 Thermodynamic properties	35
4.2.2 Movement of PI	38
4.2.3 Movement of SWCNT	43
4.2.4 Self-aggregation of CNT	45
4.3 Mechanical properties	49
4.3.1 Young's modulus of SWCNT:CL:PI	50
4.3.2 DPD reparameterization	52

	(6)
CHAPTER 5 CONCLUSIONS AND RECOMMENDATIONS	55
REFERENCES	57
APPENDIX	68
APPENDIX A ANOMALOUS DIFFUSION	69
BIOGRAPHY	70



LIST OF TABLES

Table		Page
Table 2.1	Mechanical properties of different functionalized CNT/polymer composites.	18
Table 3.1	Repulsive parameters (a_{ij}) between bead type of PI, CL, SWCNT, and fictitious bead.	22
Table 3.2	The composition of the cross-linked polyisoprene with 0-8% SWCNT loading. Noted that the sulfur cross-linker concentration is about 3%, corresponding to 3,000 beads per system.	25
Table 4.1	Comparison of topology violation between small pure PI and CL:PI systems using DPD model. Total beads: 2500, total simulation time: 100,000 steps.	33
Table 4.2	Comparison of topology violation in DPD and DPD/mSRP models of pure PI system. Total beads: 2500, total simulation times: 100,000 steps, time step: 0.001 τ .	35
Table 4.3	100% Young's modulus of cross-linked PI composite with CNT by DPD and DPD/mSRP models using the original and modified (marked with an asterisk) PI-PI repulsive parameter (a_{ii}) of 25 and 22.5, respectively.	52
Table 4.4	Computed 100% Young's modulus of the pure polyisoprene as a function of reparameterized a_{ii} term for DPD/mSRP simulation.	53
Table A1	Computed sub-diffusion coefficient (A) and sub-diffusion parameter alpha (α) of PI anomalous diffusion at different concentration of CNT for DPD/mSRP model.	69

LIST OF FIGURES

Figure		Page
Figure 1.1	Cross linking polymer. Sulfur highlighted in yellow.	1
Figure 1.2	(a) SEM image of SWCNT bundle made by Arc-discharge method and purified using concentrated acid chemistry. (b) Cylindrical structure of SWCNT.	3
Figure 1.3	SEM image of polyisoprene mixed with different CNT composites: (A) U-CNT 4 phr, (B) S-CNT 4 phr, (C) U-CNT 8 phr, and (D) S-CNT 8 phr..	3
Figure 1.4	Computational methods appropriate for treating system on different length and time scales.	5
Figure 1.5	Processing pipeline of coarse-graining of particle.	5
Figure 2.1	Distance between beads i and j is defined as r_{ij} . The d_{kl} vector is calculated by midpoint between vectors R_k and R_l . Change of direction of d_{kl} vector shown at different time steps.	8
Figure 2.2	Stress-strain curve of polymer. The Young's modulus is the slope of the curve in elastic region.	14
Figure 2.3	Schematic simulation of elongation of box along X axis. The volume of the box was kept constant.	14
Figure 3.1	DPD parameterization protocol.	21
Figure 3.2	Schematic illustration of PI bead in CG modeling. Each PI chain consists 40 beads.	24
Figure 3.3	Schematic illustration of the (5,5) SWCNT in CG modeling. Each nanotube consists 20 beads.	24
Figure 3.4	Cross-linked polymer after vulcanization.	25
Figure 3.5	Strategy for performing the simulation of mechanical properties of the SWCNT:CL:PI composite system.	26

Figure 3.6	Snapshots of pure PI system at 0%, 100%, and 200% deformation using DPD model. Only small number of PI is shown here for clarity.	28
Figure 3.7	Calculation of radius distribution function.	30
Figure 3.8	Separation displacement of CNTs and cutoff radius. The alignment of CNT was denoted by angle between the orientational vectors θ .	31
Figure 4.1	Structure of pure PI system at equilibrium state simulated by DPD model.	32
Figure 4.2	Structure of CL:PI system at equilibrium state simulated by DPD model. Sulfur cross-linker beads highlighted in yellow.	33
Figure 4.3	Number of crossing events of pure PI system at different equilibration time steps. Total simulation time: 10,000 steps.	34
Figure 4.4	Relationship between total energy of SWCNT:CL:PI composite systems and simulation steps during energy minimization calculated by DPD/mSRP model.	36
Figure 4.5	Relationship between total energy of 2% SWCNT:CL:PI composite system and simulation steps during equilibration calculated by DPD/mSRP model.	37
Figure 4.6	Simulated structure of 2% SWCNT:CL:PI composite system in equilibrium state calculated by DPD model. Nanotubes shown in green.	37
Figure 4.7	MSD of PI during system equilibration at SWCNT concentrations of 0%, 2%, 4%, 6%, and 8%, calculated by (a) DPD and (b) DPD/mSRP models.	39
Figure 4.8	MSD of PI under longitudinal deformation at SWCNT concentrations of 0%, 2%, 4%, 6%, and 8%, calculated by (a) DPD and (b) DPD/mSRP models.	40
Figure 4.9	RMS end-to-end distance of PI at equilibrium at SWCNT concentrations of 0%, 2%, 4%, 6%, and 8%, calculated by (a) DPD and (b) DPD/mSRP models.	41

Figure 4.10	RMS end-to-end distance of PI under longitudinal deformation at SWCNT concentrations of 0%, 2%, 4%, 6%, and 8%, calculated by (a) DPD and (b) DPD/mSRP models.	42
Figure 4.11	MSD of SWCNT during longitudinal deformation at different concentrations of SWCNT: 2%, 4%, 6%, and 8%, calculated by (a) DPD and (b) DPD/mSRP models.	44
Figure 4.12	Clockwise from top left: aggregated bundle of SWCNTs of 2%, 4%, 6%, and 8% mixtures at equilibrium state calculated by DPD/mSRP model.	45
Figure 4.13	Radial distribution function $g(r)$ of CNT for typical SWCNT:CL:PI composite system calculated by DPD/mSRP model. Cutoff for CNT cluster distribution is shown.	46
Figure 4.14	Average size distribution of SWCNT bundles at equilibrium state of composite calculated by DPD/mSRP model.	47
Figure 4.15	Elongation of 2% SWCNT aggregates at (a) 100% and (b) 200% strain calculated by DPD/mSRP model. The identified CNT bundles highlighted in green.	48
Figure 4.16	The orientational order parameter of CNT (SCNT) with respect to the longitudinal deformation direction during the strain evolution calculated by DPD/mSRP model.	49
Figure 4.17	Stress-strain curve of SWCNT:CL:PI composite systems at 0-8 % SWCNT calculated by DPD model.	51
Figure 4.18	Stress-strain curve of SWCNT:CL:PI composite systems at 0-8 % SWCNT calculated by DPD/mSRP model.	51
Figure 4.19	100% Young's modulus as a function of SWCNT concentrations by DPD and DPD/mSRP models using the original and modified (marked here with asterisks) PI-PI repulsive parameter (a _{ii}) of 25.00 and 22.50.	54

LIST OF ABBREVIATIONS

Symbols/Abbreviations	Terms
α	Gaussian random number
γ	Dissipative parameter
δ	Hildebrand solubility parameter
$\delta\tau$	Time step
Δ	Change
ΔL	Change in length
$\dot{\epsilon}$	True strain rate
θ	Angle
τ	Units of time step
π	Pi constant
ρ	Density
Σ	Summation
σ	Noise parameter and elongation tensile
τ	DPD time unit
\vec{v}	Velocity unit
χ	Flory-Huggins parameter
ω	Scaling factor
%	Percent
/	Per
A	Cross-sectional area
BR	Polybutadiene
E	Energy
F	Force
F_C	Conservative force
F_D	Dissipative force
F_R	Stochastic or random force
FEM	Finite element method
CB	Carbon black

CCB	Conductive carbon black
CET	Crystal elasticity theory
CG	Coarse-grained modeling
CL	Cross-linking
CL:PI	Cross-linked polyisoprene
CNT	Carbon nanotube
D	Diffusion coefficient
d_c	Cutoff radius
DPD	Dissipative particle dynamics
DPD/mSRP	Dissipative particle dynamics/modified segmental repulsive potential
DWCNT	Double-walled carbon nanotube
$g(r)$	Radial distribution function
IR	Infrared spectroscopy
LAMMPS	Large-scale Atomic/Molecular Massively Parallel Simulator
L_0	Initial length
MC	Monte Carlo
MD	Molecular dynamics
MDPD	Multibody DPD
MM	Mechanical mechanics
MSD	Mean-squared displacement
mSRP	Modified segmental repulsive potential
MWCNT	Multi-walled carbon nanotube
NBR	Nitrile butadiene rubber
NMR	Nuclear magnetic resonance
NR	Natural rubber
OVITO	Open Visualization Tool
PA6	Polycaprolactam
PAMAM	Polyamidoamine
PC	Polycarbonate

PE	Polyethylene
PEE	Polyester elastomer
phr	Parts per hundred rubber
PI	Polyisoprene
PMMA	Poly(methyl methacrylate)
PP	Polypropylene
PP+NBR	Polypropylene and nitrile butadiene rubber
PPF	Polypropylene fumarate
PS	Polystyrene
r_c	Cutoff radius
r_{ij}	Distance between beads i and j
$\langle R_{EE} \rangle$	Root mean-squared end-to-end distance
RMS	Root mean-squared
S	Sulfur agent
S_{CNT}	Orientalional order parameter of CNT
SEM	Scanning electron microscopy
SRP	Segmental repulsive potential
SWCNT	Single-walled carbon nanotube
SWCNT:CL:PI	Cross-linked polyisoprene mixed with single-walled carbon nanotube
SWCNT/PI	Single-walled carbon nanotube-reinforced polyisoprene vulcanizate
T	Temperature
TEM	Transmission electron microscope
TV	Topology violation
TWCNT	Triple-walled carbon nanotube
vdW	van der Waals
VMD	Visual Molecular Dynamics
XRD	X-ray diffraction technique

CHAPTER 1

INTRODUCTION

1.1 Statement of Problems

Natural rubber (NR) has been widely used in the industry due to its unique, for example, elasticity, low cost, light weight, and ductility.(1–3) A polymer form of NR is polyisoprene (PI), which is characterized as elastomer. One of the important feature of elastomer is the toughness, which represents the hardness and strength of material. The comprehensive strength can be determined using several parameters, for example, the Young's modulus, bulk modulus, and shear modulus or modulus of rigidity. The Young's modulus or elastic modulus was preferred and used to quantify the comprehensive strength of elastomer.(4) The experimental test to measure the Young's modulus is an elastic deformation, where the ratio between stress and strain are determined continuously until the sample has cracked. Previous studies have shown that the Young's modulus accurately determined the tensile elasticity of polymer.(5–7)

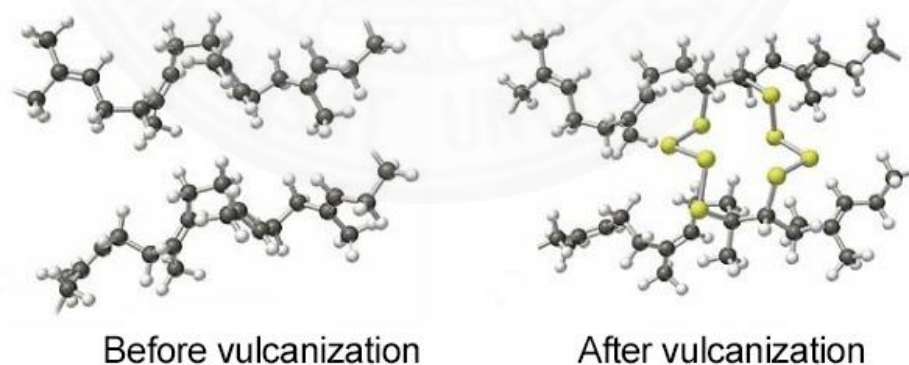


Figure 1.1. Cross-linking polymer. Sulfur highlighted in yellow.

The force resistance of NR, compared to other elastomers, is still poor and need to be enhanced.(8,9) One simple idea to overcome this shortcoming is by adding polymer additive or reinforcing filler. Synergistic combination between flexibility of rubber and rigidity of reinforcement filler leads to an improvement of mechanical properties of rubber or elastomer compound. In industrial process, vulcanization is mostly used. **Figure 1.1** shows the structure of cross-linked polymers that used sulfur (S) as cross-linker. As can be seen from **Figure 1.1**, the polymer chains are linked by sulfur cross-links agent at high temperature. The cross-link through the sulfur bridge has improved polymer properties drastically.(10,11) Besides sulfur agents, graphene sheet (GS), an allotrope of single layer of carbon atoms, and carbon black (CB), a colloidal form of carbon obtained by thermal decomposition of hydrocarbon, were used.(12,13) Nowadays, GS and CB are popular due to easy accessibility and low cost. Even though CB can enhance the strength of material, but it is not sufficient to tackle the poor mechanical properties in NR. Other choice is the single-walled carbon nanotube (SWCNT), a tube-shaped carbon nanomaterial as shown in **Figure 1.2**. SWCNT composed of benzene rings as repeating unit, which are orderly arranged in a cylindrical shape. Each carbon atom is connected to neighboring atoms through a covalent bond. Zhang *et al.* and Khan *et al.* reported that the SWCNT with high aspect ratio can reinforce the polymeric system.(14,15) The strength of SWCNT is much higher than that of other fibrous additive materials. Therefore, SWCNT can be used for enhancement of mechanical properties of NR.

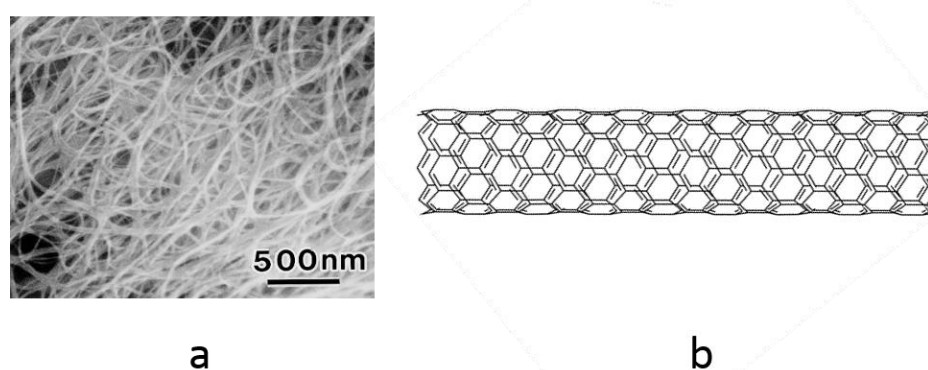


Figure 1.2. (a) SEM image of SWCNT bundle made by Arc-discharge method and purified using concentrated acid chemistry. (b) Cylindrical structure of SWCNT.

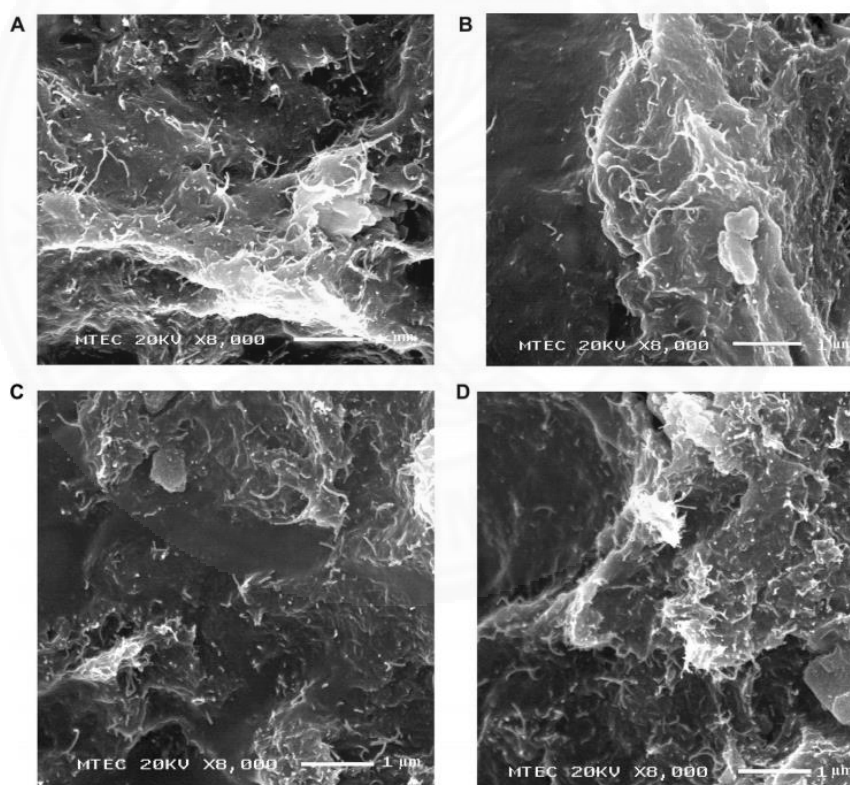


Figure 1.3. SEM image of polyisoprene mixed with different CNT composites: (A) U-CNT 4 phr, (B) S-CNT 4 phr, (C) U-CNT 8 phr, and (D) S-CNT 8 phr. Sae-Oui *et al.* (7)

Sae-Oui *et al.* studied the reinforcing efficiency of CB and SWCNT in NR composite.(7) They reported the Young's modulus and the tensile strength of NR that mixed with CB and SWCNT at different concentrations: 0%, 2%, 4%, 6%, and 8%. **Figure 1.3** shows the SEM image of SWCNT/PI vulcanizate for 4 phr and 8 phr of filler. Their experimental results showed that the mechanical strength of SWCNT/PI composite is much more than those of CB/PI and conductive CB/PI. Understanding the effect of SWCNT on the NR nanocomposites is essential for developing of promising efficient polymeric material.

It is challenging to investigate property of SWCNTs that resulting in the enhancement of mechanical strength of polymer. The powerful experimental techniques, for example, the infrared spectroscopy (IR), the nuclear magnetic resonance (NMR), and the scanning electron microscopy (SEM) are generally used for structural characterization. At this stage, where the experimental study has reached the limit, an alternative choice is a computational technique. Testing an experimental condition by simulation is much cheaper and quicker than experiment. One can gain atomistic insight into molecular structure using the molecular dynamics (MD) simulation. MD simulation has been widely used to study the time-dependent structural behavior such as the fluctuational and conformational change in protein and polymer.(16,17) However, applying the MD simulation to full atomistic-based problem is time consuming. In our case, where PI composite is simulated, the number of all atoms in simulated system beyond millions of atom. To simplify computational complexity in full atomistic simulation, some atomistic details are neglected.(18) The coarse-grained modeling is developed for simulation at long time and large scale (**Figure 1.4**).(18,19) We chose coarse-grained (CG) modeling instead of MD simulation.

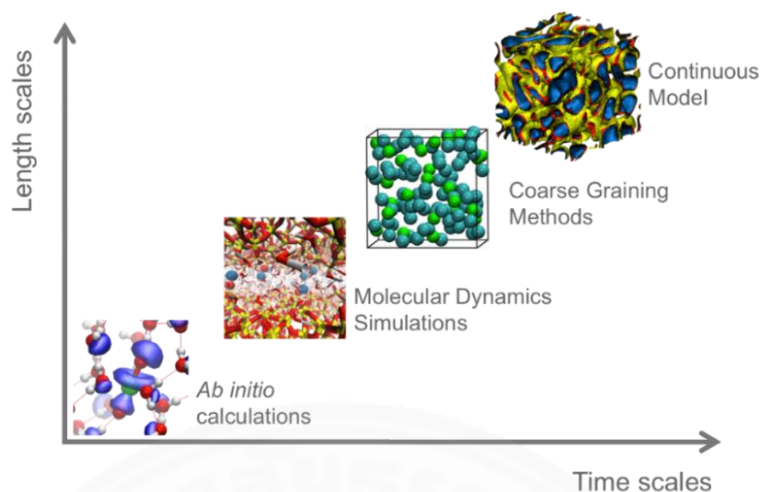


Figure 1.4. Computational methods appropriate for treating system on different length and time scales.

Basic concept of CG model is that the degrees of freedom during simulation can be integrated over.(18,20) To deal with CG model, one simulates the lump of atom or molecular fragment instead of simulating a single atom (**Figure 1.5**). Therefore, CG effectively reduces the computational cost and allows us to expand the size of studied system to be at the longer time and the larger scale.(18) CG model with some atomistic detail was therefore chosen and preferred for PI composite simulation.

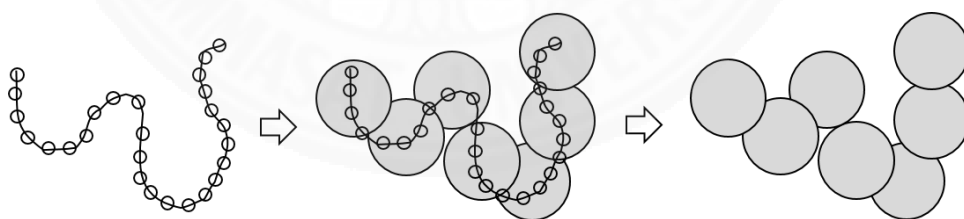


Figure 1.5. Processing pipeline of coarse-graining of particle

Applying CG modeling to the problem of polymeric system is possible by including the fluid dynamics.(21) The coarse-grained dissipative particle dynamics (DPD) model includes the hydrodynamic property of particles.(22) DPD is appropriately considered as a mesoscale modeling technique for dynamical and rheological simulations of polymer. We selected the DPD simulation as our model to predict the

Young's modulus of the SWCNT:CL:PI composite system. With performance of DPD model, we utilized DPD to investigate the role of structural change of self-aggregation of SWCNT in the mechanical strength of PI composite. Moreover, the entanglement of PI is considered. The topological failure of polymer during simulation was reduced by applying the modified segmental repulsive potential. For further study of PI simulation, we parameterized the PI interaction parameter for quantitative prediction of the Young's modulus.

1.2 Objectives

The goals of this research are as follows:

1. To understand the enhancement in mechanical properties of NR mixed with SWCNTs by means of DPD simulation.
2. To study the role of nanotubes in the morphology and mechanical strength of PI composite.
3. To compare the performance between DPD and DPD/mSRP models on the prediction of mechanical properties of rubber composite system.
4. To propose an efficient computational scheme for investigation of the mechanical properties of filled PI composite system.
5. To identify the optimal PI-PI interaction parameter for the modified segmental repulsive DPD model.

1.3 Thesis organization

Chapter 1 introduces the statement of problems and covers the objective and thesis organization.

Chapter 2 explains the theory and theoretical technique used in this research; DPD, mSRP, the Young's modulus, and topology violation. This chapter also reviews the previous studies of investigation of mechanical properties of rubber.

Chapter 3 describes the research methodology for simulating mechanical properties of PI composite, DPD method, and technique for post-simulation analysis.

Chapter 4 reports and discusses computational results, including structural behavior and dynamical properties of PI composites. The discussions of prediction of mechanical properties using DPD and DPD/mSRP models in comparison with the experimental result are reported.

Chapter 5 concludes the remarkable point and recommendation.

CHAPTER 2

REVIEW OF LITERATURE

2.1 Theoretical background

2.1.1 Dissipative particle dynamics

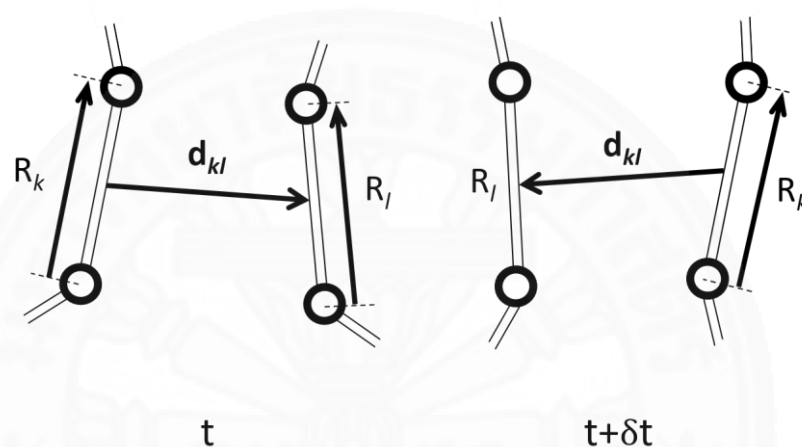


Figure 2.1. Distance between beads i and j is defined as r_{ij} . The \mathbf{d}_{kl} vector is calculated by midpoint between vectors \mathbf{R}_k and \mathbf{R}_l . Change of direction of \mathbf{d}_{kl} vector shown at different time steps.

The DPD model defines a group of atoms or monomer units as a single bead. The spring interaction of bead i and j is given by the DPD expression, which is the sum of three force terms, as given by **Equation 1**. The DPD expression comprises direct conservative (repulsion, F_C), dissipative (friction, F_D), and stochastic (random, F_R) forces, which are considered within the global cutoff radius of a sphere (r_c).⁽²²⁾

$$\mathbf{F}_{DPD} = \sum_{i,j} (\mathbf{F}_C + \mathbf{F}_D + \mathbf{F}_R)_{ij} \quad 1$$

We focused in F_C , which acts as soft repulsion between beads i and j . The F_C term is chosen to linearly decrease as bead separation increases. Furthermore, the distance between two consecutive beads (r_{ij}) is compared with the global cutoff

radius ($r_c = 1.0$). When r_{ij} beyond the cutoff distance r_c , the pairwise repulsive interaction and force are zero, and the momentum is conserved throughout simulation.

$$\mathbf{F}_C = a_{ij}\omega(r_{ij})\hat{\mathbf{r}}_{ij} \quad 2$$

where a_{ij} , ω , $\hat{\mathbf{r}}_{ij}$ are force constant, weight function, and unit vector of bead separation, respectively. Additionally, ω is the relation between distance (r_{ij}) and the global cutoff radius separation (r_c), given by

$$\omega(r_{ij}) = 1 - \frac{r_{ij}}{r_c} \quad 3$$

Depending on the direction of travel of any two beads, direction r_{ij} represents the bead-bead distance.

$$\mathbf{F}_D = -\gamma\omega_D^2(r_{ij})(\hat{\mathbf{r}}_{ij} \cdot \mathbf{v}_{ij})\hat{\mathbf{r}}_{ij} \quad 4$$

$$\mathbf{F}_R = \sigma_R\omega_R(r_{ij})\theta_{ij}\hat{\mathbf{r}}_{ij} \quad 5$$

Forces \mathbf{F}_D and \mathbf{F}_R are given by **Equations 4** and **5**, respectively. The dissipative force \mathbf{F}_D is governed by a dissipative scaling factor (γ), weight function (ω), and the relative velocity (\mathbf{v}_{ij}). The random force \mathbf{F}_R is contributed by the noise level (σ_R) and Gaussian random number (θ_{ij}). In the usual DPD simulation, γ and \mathbf{v}_{ij} represent a friction scaling factor and the velocity vector in the i - j direction, respectively. For convenience, the simulated parameters were defined as the reduced DPD units. The DPD simulated system uses the thermal energy ($k_B T$), the DPD particle mass (m), length (l), and time step size (τ), where k_B is the Boltzmann constant and T is the temperature in Kelvin. The typical simulations are run at $k_B T = 1$, $T = 308.15$ K, and $m = 1$.(23,24) The DPD maintains the correction of hydrodynamic properties of the system because \mathbf{F}_C , \mathbf{F}_D , and \mathbf{F}_R locally conserve momentum.(22) Moreover, Español and Warren showed that the weight function of dissipative and random forces are related as **Equation 6**.(25)

$$\omega_D(\mathbf{r}_{ij}) = (\omega_R(\mathbf{r}_{ij}))^2 \quad 6$$

Therefore, the relation between γ and σ_R is expressed by **Equation 7**.

$$\gamma = \frac{\sigma_R^2}{2k_B T} \quad 7$$

In this work, all forces were computed by numerically integrating the equations of motion over time using a modified version of the velocity-Verlet algorithm with microcanonical (*NVE*) and canonical (*NVT*) ensembles.(22) This algorithm is given by **Equation 8**.

$$\begin{aligned} \mathbf{r}_i(\mathbf{t} + \Delta\mathbf{t}) &= \mathbf{r}_i(\mathbf{t}) + \Delta\mathbf{t}\mathbf{v}_i(\mathbf{t}) + \frac{1}{2}(\Delta\mathbf{t})^2\mathbf{f}_i(\mathbf{t}), \\ \tilde{\mathbf{v}}_i(\mathbf{t} + \Delta\mathbf{t}) &= \mathbf{v}_i(\mathbf{t}) + \lambda\Delta\mathbf{t}\mathbf{f}_i(\mathbf{t}), \\ \mathbf{f}_i(\mathbf{t} + \Delta\mathbf{t}) &= \mathbf{f}_i(\mathbf{r}(\mathbf{t} + \Delta\mathbf{t}), \tilde{\mathbf{v}}_i(\mathbf{t} + \Delta\mathbf{t})), \\ \mathbf{v}_i(\mathbf{t} + \Delta\mathbf{t}) &= \mathbf{v}_i(\mathbf{t}) + \frac{1}{2}\Delta\mathbf{t}(\mathbf{f}_i(\mathbf{t}) + \mathbf{f}_i(\mathbf{t} + \Delta\mathbf{t})). \end{aligned} \quad 8$$

where λ is set to 1/2 to account for the effects of stochastic interactions. This modified integration was first derived by Groot and Warren.(22)

For each time step of simulation, the forces interacting between two beads were calculated. Newton's equation of motion was then solved to obtain the final displacement and the final position at each time step until the desired condition was reached. Groot and Warren showed that the DPD is valid for reproducing the canonical ensemble (*NVT*) for hydrodynamics simulation.(22)

For the interactions within a specified chain of beads, the bond and angle forces between them were given by **Equations 9** and **10**, respectively. The bond and angle potential of all bead types were constructed to represent a valid molecular structure. K_B and K_θ refer to the force constant of the bond stretching and cosine angle bending potential, and θ is angle in degree unit organized by three consecutive beads.(26)

$$F_{jk}^B = -K_B(r_{ij} - r_0)\hat{r}_{ij} \quad 9$$

$$F_{ijk}^\theta = K_\theta(1 + \cos\theta) \quad 10$$

2.1.2 Segmental repulsive potential

2.1.2.1 Topology violation

Although the DPD model can provide details of simulation with longer time and length scales when compared with MD simulation, caution must be taken when modeling a PI network using only DPD. The soft repulsive potential of the DPD model allows for an unphysical polymer chain crossing.(27–29) Kumar and Larson studied the spring-spring interaction with Brownian motion of polymer.(30) They reported that unphysical bond crossing in polymer simulation occurs frequently, leads to topology violation (TV). For the current study, TV is defined as the number of polymer chain crossing during simulation. TV frequently occurs during system equilibration under increasing temperature and deformation simulations because the DPD does not account for the polymer chain-chain repulsion.(23,31)

2.1.2.2 Modified SRP model

To avoid TV in PI simulation, a workaround is to decrease the speed of changes of system and to decrease the temperature (kinetics energy) in order to reduce the possibility of collision between polymer chains. However, this solution is not appropriate for some specific simulation of polymer, for example, vulcanization that requires high temperature and so the TV is still possible. Therefore, self-avoiding model is considered as alternative solution.(29)

Goujon *et al.* applied the segmental repulsive potential (SRP) for mesoscopic simulation.(29) In SRP, an external force is incorporated into a conventional DPD force by adding fictitious bead between consecutive PI beads. Each fictitious bead is assigned a repulsive force acting on its neighbors. Sirk *et al.* developed modified segmental repulsive potential (mSRP) by redefining the bond-bond interaction when polymer chain crossing occurs.(23) They defined the distance

between PI-PI separations from mid bond to mid bond instead of the minimum displacement used in Goujon *et al.*(29) The modified paradigm contains an additional force term F_{kl}^{mSRP} for this pseudo potential. This was incorporated in the conventional DPD model (**Equation 1**), and is given by **Equation 11**.

$$F_{kl}^{mSRP} = \begin{cases} a_{kl}^{mSRP} \left(1 - \frac{d_{kl}}{r_c^{mSRP}} \right) \hat{r}_{kl}, & d_{kl} < r_c^{mSRP} \\ 0, & d_{kl} \geq r_c^{mSRP} \end{cases} \quad 11$$

where a_{kl}^{mSRP} is the maximum force constant between bonds k and l oriented by d_{kl} distance and r_c^{mSRP} is the mSRP bond-bond cutoff distance, set to 0.8 in DPD units in our study.

When this avoided-crossing model is used, repulsion between polymer chains depends strongly on the repulsive parameter (a_{kl}^{mSRP}). mSRP can preserve an unphysical bond crossing without affecting the structural or thermodynamics properties. Sirk *et al.* also parameterized the a_{kl}^{mSRP} parameter with the typical polymer model.(23) We then adopted their suggested parameter for our further calculation.

To determine the degree of TV in PI simulation, we computed the time-evolution of the number of chain crossings from a short simulation. Supposed that the angle (θ) of two correlated d_{kl} unit vectors from the previous step to the current step is less than 90 degrees, non-crossing of polymer chains is assumed. In contrast, if the change of vector direction is between 90 degree and 180 degree, it is assumed that the two PI chains crossed each other. This is expressed mathematically by **Equation 12**.

$$\cos(\theta) = \hat{d}_{kl}^t \cdot \hat{d}_{kl}^{t+\delta t} \quad 12$$

2.2 Young's modulus test

Although powerful experimental techniques, such as X-ray diffraction (XRD) and nuclear magnetic resonance (NMR) can resolve the atomic structure, they are inconvenient to study the change in tensile strength and tensile elasticity of polymer when opposing external forces. The Young's modulus was used in this study to determine tensile strength and tensile strain of polymer. The Young's modulus is divided into two type: an engineering and a true stress-strain. Engineering stress is the applied load divided by the original cross-sectional area of a specimen, whereas true stress is the applied load divided by the actual cross-sectional area of a specimen at that load in which the cross-sectional area is changing with respect to time. In this work, a true stress-strain is chosen. The modulus at the start of the test indicates the elasticity of a specimen. The Young's modulus can be obtained from the stress-strain curve, and is calculated by dividing the tensile stress by the extensional strain during deformation of the sample, given by **Equation 13**.

$$\text{Young's modulus} = \frac{\sigma}{\varepsilon} = \frac{F/A}{\Delta L/L_0} \quad 13$$

where σ is the uniaxial stress, ε is the strain, F is the external force applied on the system, A is a cross-sectional area, L_0 is the initial length, and ΔL is the change in length of the system under the deformation.

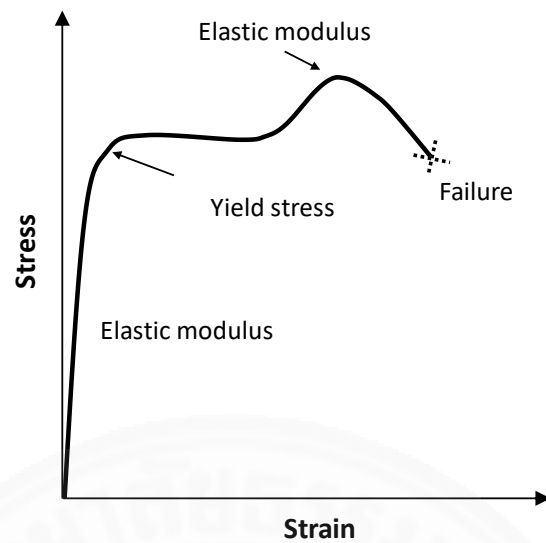


Figure 2.2. Stress-strain curve of polymer. The Young's modulus is the slope of the curve in elastic region.

Figure 2.2 shows the relation between stress and strain during deformation of a polymer. This curve can be divided into four regions: elastic region, yielding region, strain hardening region, and necking region. We consider the first region because the Young's modulus applies to the elastic modulus regime.

2.2.1 Simulation of modulus

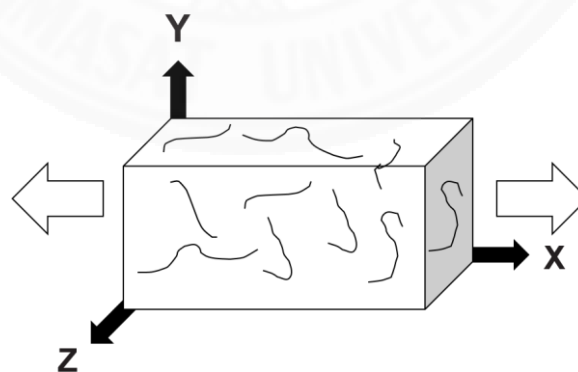


Figure 2.3. Schematic simulation of elongation of box along X axis. The volume of the box was kept constant.

To simulate the stress-strain curve and the Young's modulus of PI composite, an equilibrium PI composite system was simulated by applying 1D-longitudinal deformation to derive the stress-strain curve. An artificial extensional force is continuously applied to a PI composite cubic box under constant volume and the stress-strain relationship is recorded. The stress is the external force divided by the cross-sectional area of the polymeric system. One can directly determine the net stress by calculating the change in internal pressure, given by **Equation 14**. (32)

$$\sigma_{\text{elongation}} = -\Delta P_{xx} + \frac{1}{2}(\Delta P_{yy} + \Delta P_{zz}) \quad 14$$

where $\Delta P = P_{\text{deformation}} - P_{\text{equilibrium}}$ and denotes the specified net pressure change as the box is deformed with constant volume during the *NVT* simulation.

The stress is computed only in the x direction which the force is applied. Therefore, the stresses in y and z directions are excluded. The deformation simulation was continuously carried out at a constant true strain rate $\dot{\epsilon}$ of 0.0269 s^{-1} . The simulation was run until change of elongation has reached 200% strain. The true strain rate used in this work is in the same range of that suggested by Gao *et al*, 0.0327 s^{-1} .(33) They simulated the stress-strain curve of PMMA composite mixed with CNT using DPD model.(33) Furthermore, the length of simulated box (L) gradually increases in a non-linear fashion as a function of the number of deformation simulation steps. (34) This relation is given by **Equation 15**.

$$L(n\delta t) = L_0 \exp(\dot{\epsilon} \times n\delta t) \quad 15$$

2.3 Literature review

Enhancement of the modulus of NR properties single-walled carbon nanotube (SWCNT), double-walled carbon nanotube (DWCNT), triple-walled carbon nanotube (TWCNT), and multi-walled carbon nanotube (MWCNT) has been achieved in many ways.(4,35–43) They have been investigated as a reinforcement filler in several

novel polymer composites, enhancing properties including interfacial bonding, electrical conductance, and elastic modulus.(44,45) For example, the elastic modulus in polypropylene (PP) reinforced with DWCNT and TWCNT increases by about 22% compared with that of pure polymer.(46) Wei *et al.* studied the mechanical response of DWCNT and TWCNT under tensile load using a Scanning Electron Microscope equipped with a nanomanipulator.(47) They found that TWCNT has a lower breaking strain and stress than DWCNT, caused by the defects that arise from chemical decomposition.

Lalwani *et al.* investigated the efficiency of SWCNT and MWCNT as reinforcing agents for cross-linked polypropylene fumarate (PPF) and polypropylene and nitrile butadiene rubber (PP+NBR) composite.(48) They reported that SWCNT performs better than MWCNT because the latter has a gap between the carbon layers. The empty space decreases the stiffness.(49) Their results agreed well with those of Gao *et al.*, who studied the use of CB and CNT for promoting the mechanical strength of PI.(50) Shvartzman-Cohen *et al.* studied the self-assembly of amphiphilic block copolymers mixed with SWCNT and MWCNT using the differential scanning calorimetry (DSC) technique and reported that the SWCNT showed the cooperativity of aggregating nanotube rather than that of MWCNT.(51) This study agreed with the study of Ahir *et al.*, who investigated the alignment and self-aggregation of SWCNT in polymer.(52) The study of Zhao *et al.* also confirmed that the strength of PI nanocomposite is due mainly to self-aggregation of SWCNT, rather than contact between filler and matrix.(53)

Byrne and Gun'ko compared the Young's modulus of different polymers mixed with functionalized SWCNT and MWCNT.(54,55). They reported that the performance of the CNT, in particular that of SWCNT, depended on the purity, size, and length of the tube.(38,56) Therefore, the occurrence of self-aggregation depends on the physical properties and concentration of CNT in polymer composite. Sae-Oui *et al.* evaluated the Young's modulus and tensile strength of CL:PI and SWCNT:CL:PI composite at different type of CNT and nanotube loadings.(7) They compared the mechanical strength of CL:PI mixed with a sonicated SWCNT filler and with an

untreated SWCNT filler. Their results revealed that the mechanical properties of the SWCNT:CL:PI composite depend on the concentration, diameter, shape, and length of the SWCNT, but not on its type, their results also confirms the study of Byrne and Gun'ko.(54) They also studied the relationship between the SWCNT concentration in PI composites and their strength, and reported that the strength increased from 1.55 MPa to 4.74 MPa as the concentration increased from 2% to 8%.

Table 2.1 shows the mechanical properties of different CNT/polymer composite systems. Azam *et al.* studied the role of concentration of SWCNT in tensile strength of PI composite. They prepared SWCNT/PI nanocomposite with different concentrations of SWCNT: 0 phr, 5 phr, 10 phr, and 15 phr.(57) They found that tensile strength and elongation break decreased significantly by 18 % with the addition of 15 phr SWCNT. Moreover, as can be seen from **Table 2.1**, even at low concentration, SWCNTs is sufficient to strengthen the rubber. However, Uchida *et al.* found that adding CNTs at very high concentration reduces the mechanical strength from 19.7 GPa to 13.2 GPa.(58) They used X-Ray scattering technique to study the soft segment content and found that the reduction of the strength in PI composite is due to the phase separation of the CNT and polymer. Nah *et al.* attributed the polymer reinforcement by CNTs to the large aspect ratio of nanotube, and to effective load transfer rather than interaction of nanotube with the polymer.(59)

Table 2.1. Mechanical properties of different functionalized CNT/polymer composites.

Filler/Polymer composite	Filler content (wt%)	Y_{Polymer} (MPa)	$Y_{\text{Composite}}$ (MPa)	Year and reference
MWCNT/BR	10	1.64	2.62	2004 & (54)
MWCNT/Butyl rubber	5	2.0	3.8	2016 & (60)
MWCNT/PMMA	3	2.7	2.9	2006 & (61)
SWCNT/NBR	4	2.02	3.4	2004 & (62)
SWCNT/PA6	1.5	0.44	1.2	2005 & (63)
SWCNT/PVA	0.8	2.4	4.3	2005 & (64)
SWCNT/PAMAM	1	2.76	3.49	2008 & (65)
SWCNT/PS	0.25	1.29	1.63	2008 & (66)

Ruoff *et al.* reported the mechanical properties of armchair and zigzag SWCNTs both experimentally and theoretically by applying SEM and Crystal Elasticity Theory (CET).(67) They reported the stress-strain curves obtained from tensile-loading experiments on individual SWCNT bundles, and reported that their samples exhibited high stiffness, approximately 30 GPa, under tensile load and the low density. The diameter of the CNT filler interacting with the PI matrix played a role in the dispersion and conformational changes of the filler. Since the stress is determined by one dimensional deformation, the rod shape of the filler can restrict and obstruct polymer movement as the composite is being deformed.(38)

Although a large number of experimental studies and simulations have clarified the role of CNT in the mechanical properties of CL:PI composite, that of SWCNT remains unclear. Further work is therefore needed to understand the role of SWCNT aggregation in determining the mechanical properties of PI composite. A computational technique can be used to account for this problem. Molecular Dynamics (MD), Monte Carlo (MC) simulations, and the Finite Element Method (FEM) simulation have been used to explore characteristics including crystallization, dispersion, and interfacial interactions, and the role of polymer nanocomposite morphology in the mechanical properties.(68–70) Frankland *et al.* investigated the stress–strain response of polyethylene (PE) matrix composites reinforced with stiff (10,10) armchair SWCNTs using MD simulation.(71) They found that the CNT can increase the modulus approximately by 14%. Mokashi *et al.* used molecular mechanics (MM) simulations to study the nanotube-amorphous PE composite and demonstrated that both the PE configuration and CNT characteristics of the composite play important roles in the tensile strength.(72) WenXing *et al.* studied the Young’s moduli of SWCNT and graphite using MD simulation.(5) They applied the modified empirical potential function model and investigated the van der Waals force in nanotube. The MD results showed the Young’s modulus of SWCNT to be approximately 930 GPa, which is slightly below that of graphite by 96 GPa. Yang *et al.* compared the performance of DPD and standard MD in simulating the mechanical properties of glycidyl azido polymer.(73) The results were in good agreement with low error. For the current study, coarse-grained DPD simulation was selected because of its simplicity and accuracy.(74–76)

Even though the DPD model has been applied to many engineering polymeric systems, such as PE and PP, it has not yet been used to study SWCNT:CL:PI composites.(77–82) Because of its importance as an engineering material and the availability of experimental data, we therefore chose SWCNT:CL:PI composite as our studied system.(7,83) The effect of using SWCNT as a filler on the mechanical properties of the NR composite was also investigated. Moreover, our goal was to evaluate the performance of the DPD and DPD/mSRP models on the prediction of the Young’s modulus of the SWCNT:CL:PI at different concentration of CNT. In this study,

we parameterized, performed, and analyzed coarse-graining simulations of SWCNT:CL:PI composite using the standard DPD and DPD/mSRP models. The results of our simulation were compared with the experimental study of Sae-Oui *et al.*(7) The computational results reported in the current work has been published as Ketkaew, R.; Tantirungrotechai, Y. *Macromol. Theory and Simul* **2018**, 1700093. (84)



CHAPTER 3

RESEARCH METHODOLOGY

3.1 DPD parameterization

We parameterized the repulsive parameter for interaction between polyisoprene and carbon nanotube (PI-CNT), and between cross-linker and carbon nanotube (CL-CNT) following the protocol suggested by Chakraborty *et al.* and Groot and Warren. The protocol of derivation of parameter is illustrated in **Figure 3.1**.

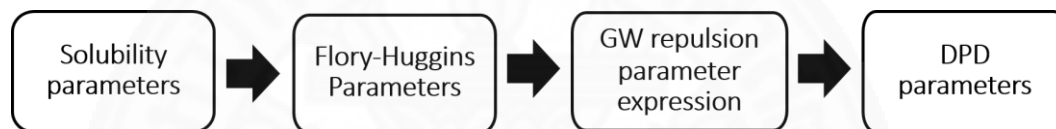


Figure 3.1. DPD parameterization protocol

We derived the Flory-Huggins (χ) parameter, which is a simplifying parameter for polymer mixing. The χ can be calculated from Hildebrand solubility parameters (δ) using **Equation 16**.

$$\chi = \frac{V_{\text{avg}}}{k_B T} (\delta_i - \delta_j)^2 \quad 16$$

The set of repulsive parameters of PI-CNT and CL-CNT beads can be obtained from the **Equation 17**. The Hildebrand solubility parameters for PI (δ_{PI}) and for SWCNT (δ_{CNT}) are 16.4 and 18.4 (J/cm³)^{1/2}, respectively. The V_{avg} term is the average molar volume of beads i and j . We determined its value to be 123.4 Å³ based on the volume of a PI monomer unit from atomistic simulation, 49.37 Å³ and volume of CNT bead that is roughly four times that of PI monomer, 199.47 Å³.⁽⁸⁵⁾ The temperature was set to 308 K. The relation between those parameters can be estimated as following equation depending on the number of densities of system.

$$\chi_{\rho=3} = (0.286 \pm 0.002)\Delta a_{ij} \quad 17$$

The Groot and Warren repulsive parameter expression (**Equation 17**) provides the linear relationship between the Flory-Huggins parameter and DPD interaction parameter, based on a number density (ρ) of $3r_c^{-3}$, which is a typical setup for DPD simulations.(22) The density of system is given by the number of all bead over volume of system. All DPD repulsive parameters were listed in **Table 3.1**. Additionally, the a_{ij} parameters can be fine-tuned to achieve a good prediction, which agree with experimental value.

Table 3.1. Repulsive parameters (a_{ij}) between bead type of PI, CL, SWCNT, and fictitious bead.

Repulsive parameter	PI	CL	SWCNT	midpoint of the non-neighboring segment
PI	25.00	24.05	25.417	-
CL		25.00	25.417	-
SWCNT			25.00	-
midpoint of the non-neighboring segment				60.00

To represent a chain of elastic polymer, all PI beads in each polymer chain were connected by harmonic bonding and angle bending terms. We employed a K_B value of $225k_B T$ and an R_0 value of $0.85r_c$ as recommended by Liba *et al.*(86) for harmonic bonding potential, and K_θ of $5k_B T$ for cosine angle potential term, as suggested by Zhou *et al.*(87) To ensure that the CNT is stiff and rigid, its K_B and K_θ parameter must be much greater than those of PI. We adopted the CNT parameters of Chakraborty *et al.*, which used values of $500 k_B T$ for K_B and $100 k_B T$ for K_θ .(88) The

harmonic angle potential has a minimum at 180 degrees corresponding to the linear CNT structure.

Sirk *et al.*, who developed DPD/mSRP model, recommended a value of $60k_B T$ for a_{kl}^{mSRP} based on the work of Goujon and a cutoff distance r_c^{mSRP} of $0.8r_c$.⁽²³⁾ Their mSRP parameter has proven to be suitable with typical polymer. Our preliminary simulation confirmed previous findings that these values significantly reduced the number of polymer crossing events. The dissipative and stochastic forces in the DPD model were tuned by the dissipative (γ) and the noise (σ) parameters. Following Wang *et al.* and Sirk *et al.*, the recommended values of the γ and σ parameters for polymer composites were set to 4.5 and 3.0 DPD units, respectively.^(23,80) These values were kept fixed for all DPD simulations. Other parameters were manipulated by the global DPD parameter. The random seed number of DPD was set to 343,879 and the cut-off distance is 1.

3.2 DPD bead modeling

The DPD bead of the PI, SWCNT, and S agent were differently constructed depending on the chemical identity, conformational behavior, and shape of structure.

3.2.1 Modeling of PI

The monomer in PI chain was replaced by a DPD bead. All the beads were constructed with the same size from 13 atoms (including all of carbon and hydrogen in isoprene-monomer). Sirk *et al.* studied the thermodynamics relation between solubility parameter and characteristic chain length (N) of polymer.⁽²³⁾ They systematically determined the suitable number of PI bead and reported the suggestion of N=40 for typical polymer. In this work, the atomistic model for PI therefore was built with 40 monomers. There are five carbon atoms per monomer (see **Figure 3.2**). Four carbon atoms were connected sequentially as a backbone and the fifth carbon was connected to the backbone as a side chain. It was assumed that the center of the monomer lies on the center of the carbon-carbon double bond.

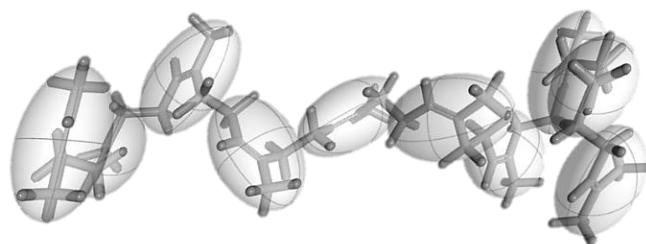


Figure 3.2. Schematic illustration of PI bead in CG modeling. Each PI chain consists 40 beads.

3.2.2 Modeling of SWCNT

SWCNTs used in our simulation were modelled using a tubular model in which each nanotube was constructed from repeating circular unit consisting of 20 beads (see **Figure 3.3**). Each nanotube bead was attached to two neighbors. All coarse-grained nanotube beads have the same size. In the absence of experimental data, all PI and CNT beads can be modeled with the same size. So that an average bead volume of beads PI and CNT would be used to compute the Flory–Huggins parameter.(85,89)

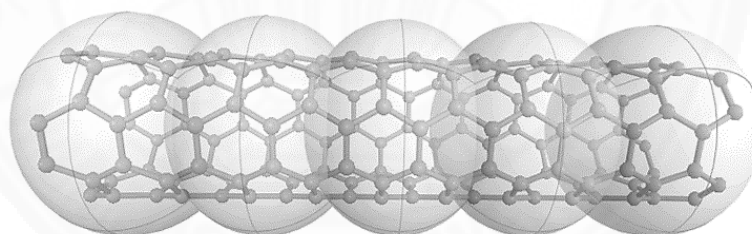


Figure 3.3. Schematic illustration of the (5,5) SWCNT in CG modeling. Each nanotube consists of 20 beads.

3.2.3 Modeling of cross-link

To represent the cross-link between PI chains, S cross-linking agents were modeled as a single-site bifunctional particles. S agents were used to link two PI chains in a random fashion. **Figure 3.4** shows the schematic representation of connection between polymer chains.

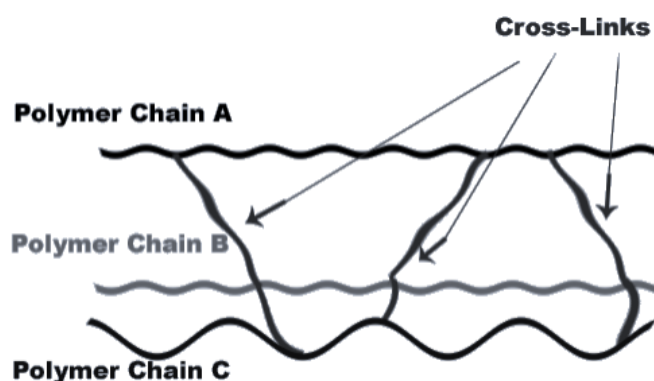


Figure 3.4. Cross-linked polymer after vulcanization.

Table 3.2. The composition of the cross-linked polyisoprene with 0-8% SWCNT loading. Noted that the sulfur cross-linker concentration is about 3%, corresponding to 3,000 beads per system.

System	No. of bead per chain	No. of chain at various concentration of SWCNT				
		0%	2%	4%	6%	8%
PI	40	2500	2450	2400	2350	2300
SWCNT	20	0	100	200	300	400

We simulated pure polyisoprene (PI), cross-linked polyisoprene (CL:PI), and cross-linked polyisoprene mixed with single-walled carbon nanotubes (SWCNT:CL:PI) composite systems. Suitable amount of S agent for PI cross-linking was considered because the overabundant S agents make a phase separation between cross-linker and polymer matrix.⁽⁹⁰⁾ Previous study showed that 3% of S is sufficient to represent the vulcanization.^(85,88)

In addition, SWCNT:CL:PI composite was studied with different concentration of CNT: 2%, 4%, 6%, and 8%. Data on number of bead type and number of chain used in all simulations are reported in **Table 3.2**.

3.3 Simulation protocol

The content of this part is simulation approach for PI composite. Throughout running coarse-grained DPD simulation, the coordinate of all particles in studied system were stored in the topology file. This file also contains their important physical information, including bond and angle interactions.

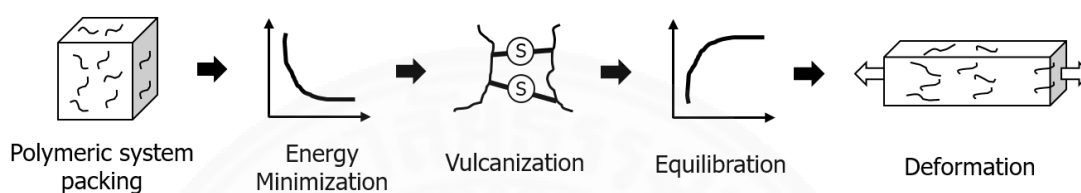


Figure 3.5. Strategy for performing the simulation of mechanical properties of the SWCNT:CL:PI composite system.

3.3.1 Molecular configuration setup

Setup of system configuration is an important stage in which a good starting point can help to simulate the following stages with more speed. The initial structure of PI composite was generated for dynamics simulation. The SWCNT:CL:PI composite system considered in this work contained 100,000 beads. Periodic boundary condition (PBC) was used in our simulation for approximating larger polymeric system by using a small unit cell. The size of box is $L_x \times L_y \times L_z = 32.183 \times 32.183 \times 32.183 (r_c)^3$, where r_c was derived from the density of real polymer. All PI, CL, and SWCNT beads were randomly filled into a cubic box using Packmol program.⁽⁹¹⁾ The concentration of SWCNT was varied from 0.0 to 8.0 % with an increment of 2.0, as shown in **Table 3.2**. Since the simulation is coarse-grained, the tolerance of distance between beads should be larger than that generally used for all atomistic-based model. The tolerance value was set to 2, suggested by program developer.⁽⁹¹⁾ The random initial point for minimization in Packmol was also used. Then, all coordinates were converted to LAMMPS format using the Moltemplate package.⁽⁹²⁾ The structural information of SWCNT:CL:PI was also transformed, including the cartesian coordinate, bond distance,

and bond angle. The Large-scale Atomic/Molecular Massively Parallel Simulator (LAMMPS) was used to perform all of DPD simulations.(93)

3.3.2 Dynamics simulation

Initial coordinates constructed by random packing have poor contacts, causing high forces and energies. Therefore the first stage of dynamics simulation usually is the energy minimization. Then the simulation is carried out using the microcanonical (*NVE*) ensemble, where the number of bead N , volume of system V , and energies E are fixed. The purpose of this step is to arrange configuration of particles. Therefore, position of bead, bond distances, and bond angles would be optimized for production simulation. The simulation was performed at temperature of 308 K. The simulation time step $\delta\tau$ was 0.001τ , where $\tau = (mr_c^2/k_B T)^{1/2} = 0.269$ ns.

After energy minimization, the simulation was followed by vulcanization. We mimicked this process by launching the cross-link reaction every 100 time steps with a reaction probability of 0.5.(93,94) The reaction proceeded until all possible bonds have been formed. The simulation of CL:PI system was conducted until the system has reached an equilibrium state. During this simulation the temperature of the system is being controlled to high temperature. The temperature was linearly increased from 0 K to 423 K within 100,000 steps of DPD simulation.

Equilibration stage is used to stabilize the total energy of system by balancing the kinetic (E_p) and potential (E_k) energies. The E_p must be equilibrated with the E_k . This means that the E_k would be transferred to potential energy until the system has reached an equilibrium. Heating and equilibration at fixed temperature permit the state of system to escape the local minima to another with low energy barriers. This simulation was carried out for 10^6 steps in the canonical ensemble (*NVT*) with constant number of bead, volume, and temperature. The Langevin thermostat is used to keep the temperature constant at 308 K. Following the Langevin dynamics simulation, the Nose-Hoover *NVT* simulation was continued for another 10^6 time steps to ensure that the system has reached equilibrium or steady state in which the

dynamics property of system remains constant over simulation time.(95,96) The velocity Verlet integration scheme was used throughout the simulation.

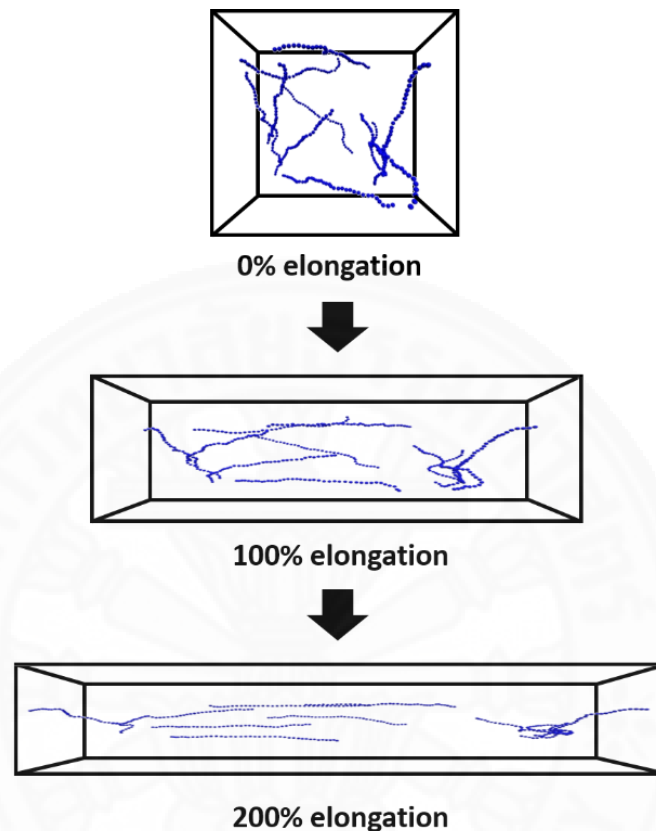


Figure 3.6. Snapshots of pure PI system at 0%, 100%, and 200% deformation using DPD model. Only small number of PI is shown here for clarity.

Elongation simulations of pure polyisoprene (PI), cross-linked polyisoprene (CL:PI), and SWCNT:CL:PI composite systems were performed with *NVT* ensemble until the box length along the pull direction has reached 200% elongation. **Figure 3.6** shows the snapshot of simulated system at 0%, 100%, and 200% strain. This Deformation can be done using *fix deform* module in LAMMPS program package. Additionally, remapping coordinate system must be taken for this simulation stage in order to avoid the collapse between beads.

3.4 Post-simulation analysis

3.4.1 Molecular visualization

All DPD results were visualized and analyzed using several programs. We use the visual molecular dynamics (VMD) to compute the radial distribution function of PI.(97) Root mean-squared displacement and root end-to-end displacement were computed using LAMMPS.(93) The Open Visualization Tool (OVITO) molecular graphic viewer was used to display all composite systems and nanocomposite arrangement during both the equilibration and deformation simulations.(98)

3.4.2 Mean-squared displacement

Mean-squared displacement, MSD is a time-evolution of measurement of deviation of the position of beads. One can use RMSD to measure the flexibility of PI and SWCNT in an energy minimization, an equilibration, and a deformation simulations. The slope of MSD is directly related to the diffusion coefficient (D) of the diffusing beads and time step (τ).

$$MSD = 6D\tau \quad 18$$

3.4.3 Root mean-squared end-to-end distance

Root mean-squared end-to-end distance, $\langle R_{EE} \rangle$ is yet another root mean-squared parameter, which is a calculation of distance of linear polymer chain averaged over all conformations of the chain. $\langle R_{EE} \rangle$ corresponds to the vector connecting the first and the last beads of the polymer. For a freely jointed polymer chain consisting of N beads and chain length is L , the $\langle R_{EE} \rangle$ is given by **Equation 19**.

$$\langle R_{EE} \rangle = \sqrt{NL} \frac{(1 + \cos\theta)}{(1 - \cos\theta)} \quad 19$$

Where θ is fixed bond angle in degree. $\langle R_{EE} \rangle$ can represent the average distance between the first and the last bead of CNT and PI chain as the directional change along simulation time.

3.4.4 Radial distribution function

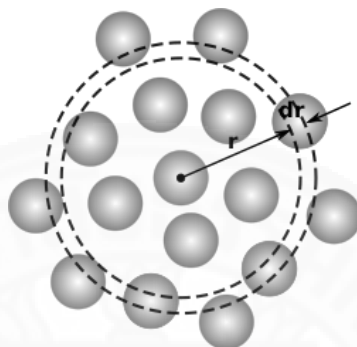


Figure 3.7. Calculation of radius distribution function

Radius distribution function or pair correlation function, $g(r)$, is one of useful parameter for analyzing morphology of system. It is the probability of finding a pair of atoms a distance r apart relative to the probability for a completely uniform distribution. $g(r)$ is calculated for each frame and then averaged. It was used in this work for cluster analysis of nanotube.

3.4.5 Orientational order parameter

The description of morphology of SWCNT involves the analysis of orientational order. The nanotube orientation along longitudinal deformation direction is monitored as a function of strain. The orientational order parameter S_{CNT} is defined based on the second order Legendre polynomial, given by **Equation 20**.

$$S_{\text{CNT}} = \langle P_2(\cos \theta) \rangle = \left\langle \frac{3\cos^2\theta - 1}{2} \right\rangle \quad 20$$

where θ is the angle between the nanotube direction and the longitudinal deformation direction. S_{CNT} is useful for studying the configuration of CNT aggregation. This parameter indicates the alignment of nanotube during deformation.

3.4.6 Cluster analysis

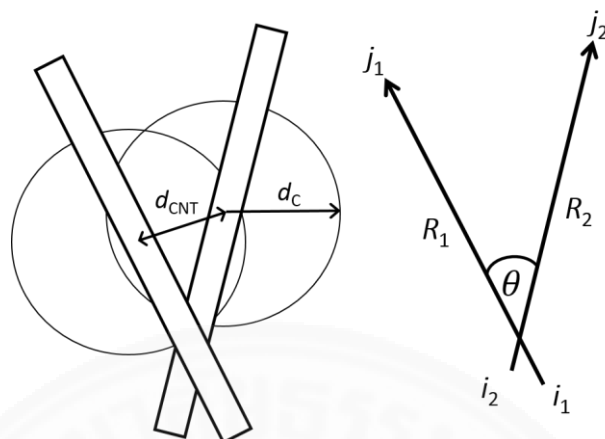


Figure 3.8. Separation displacement of CNTs and cutoff radius. The alignment of CNT was denoted by angle between the orientational vectors θ .

We analyze the self-aggregation or self-assembly of SWCNT using a cluster analysis technique. Two criteria: the distance-based neighbor cutoff and alignment of nanotube were used for clustering SWCNTs. The first one is screening of the displacement of nanotube and the nearest neighbors. The displacement between the two nanotubes defined as center of tube to center of tube is computed and compared to a cutoff radius (d_c) in defined region, where d_c was adopted from the first $g(r)$ peak.

CHAPTER 4

RESULTS AND DISCUSSION

4.1 Entanglement property

4.1.1 Effect of cross-links

The final structures of the simulated PI and CL:PI systems in equilibrium state are shown in **Figure 4.1** and **Figure 4.2**. The latter shows the dispersion of sulfur (S) cross-linkers in the polymer matrix, used to promote entanglement of PI. To investigate the role of topology violation (TV) in our studied polymeric system, we determined the TV from the number of PI chain crossings in small representative pure PI (without S agents) and CL:PI systems using the DPD model. Both systems contain 2,500 beads, but in the CL:PI, 3% of beads are replaced by S cross-linker beads. **Table 4.1** compares the number of PI chain crossings during system equilibration and deformation. The number of PI chain crossings in the CL:PI system were at least an order of magnitude lower than in the pure PI system.

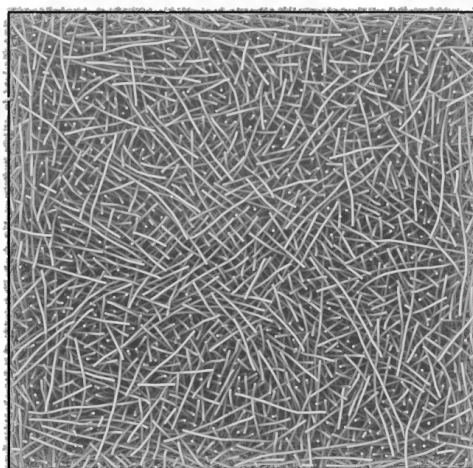


Figure 4.1. Structure of pure PI system at equilibrium state simulated by DPD model.

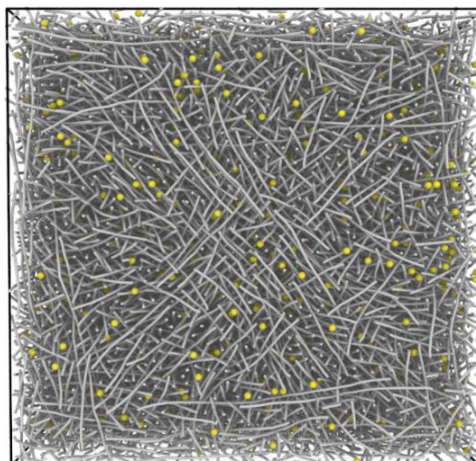


Figure 4.2. Structure of CL:PI system at equilibrium state simulated by DPD model. Sulfur cross-linker beads highlighted in yellow.

Table 4.1. Comparison of topology violation between small pure PI and CL:PI systems using DPD model. Total beads: 2500, total simulation time: 100,000 steps.

Simulation	Number of PI chain crossings	
	PI	CL:PI
Equilibration	98,953	18,430
Deformation	159,006	25,871

While TV is a major issue when simulating a polymeric system, especially elastomer, the second factor affecting the movement of the PI chain is the speed of particles. In the DPD simulation, the time step ($\delta\tau$) dependence of TV was investigated. **Figure 4.3** shows the relationship between the number of PI chain crossings and $\delta\tau$ for the pure PI system 2,500 beads. For system equilibration, we used four time steps (τ): 0.1, 0.01, 0.001, and 0.0001. The number of PI chain crossings and $\delta\tau$ were confirmed to be correlated. As the time step was reduced from 0.1 τ to 0.01 τ , the number of PI chain crossings reduced from 2,860 to 1,706, and further to 1,504 and to 1,302 at time step of 0.001 τ and 0.0001 τ , respectively. For energy equilibration,

the simulation time must be sufficient to ensure that equilibrium has been reached. Our results confirm those of Sirk *et al.*, who reported that the number of PI chain crossings quickly increased when $\delta\tau$ was greater than 0.01τ .(23) All further DPD simulation set $\delta\tau = 0.001\tau$ because this yields a small TV whilst ensuring fast equilibration.

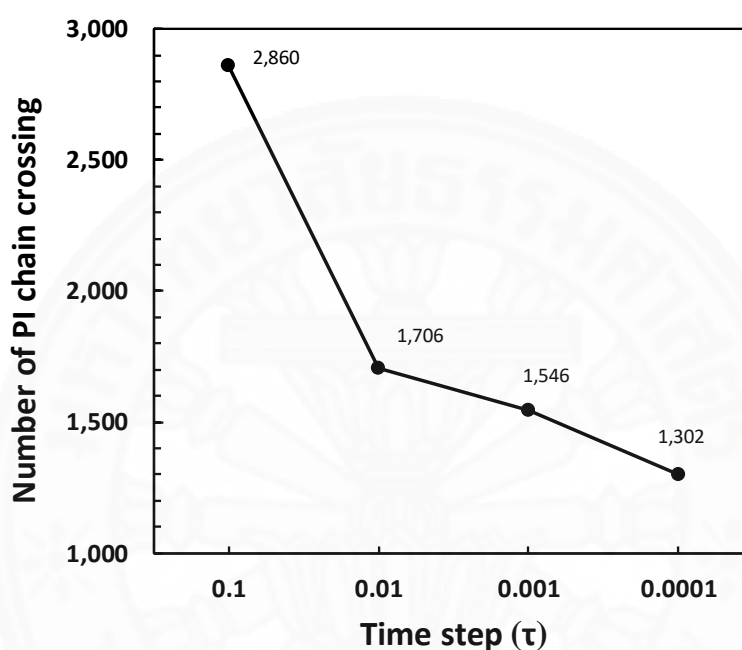


Figure 4.3. Number of crossing events of pure PI system at different equilibration time steps. Total simulation time: 10,000 steps.

4.1.2 Effect of self-avoiding model

The effect of self-avoiding was also studied. We monitored PI chain crossing from the evolution of the PI-PI direction over time. DPD and DPD/mSRP models were applied to a small pure PI system.

Table 4.2. Comparison of topology violation in DPD and DPD/mSRP models of pure PI system. Total beads: 2500, total simulation times: 100,000 steps, time step: 0.001 τ .

Simulation	Number of PI chain crossing	
	DPD	DPD/mSRP
Equilibration	98,953	1,484
Deformation	159,006	2,687

Table 4.2 shows the number of PI chain crossings during equilibration and deformation of a pure PI system in the DPD and DPD/mSRP models. The DPD model yielded the number of crossing event at least two orders of magnitude greater than those of DPD/mSRP model. The number of PI chain crossings in the DPD/mSRP model suggested that the model produced PI chain folding, inhibiting PI chain crossing. However, a small number of chain crossings persisted due to random, uncontrolled movement of PI. The rapidity of directional translocation of spring-spring beads in both models also produces TV.

Our results are consistent with those of Trofimov, who used modified Multi-body dissipative particle dynamics (MDPD) to study liquid mixtures.⁽⁹⁹⁾ In the current study, the preliminary PI simulation results showed that cross-linking of PI and the segmental repulsive potential model are necessary for modeling entanglement in a PI composite system.

4.2 Thermodynamics and structural stabilities

4.2.1 Thermodynamic properties

We examined the effect of varying the concentrations of nanotube on the total energy of a single-walled carbon nanotube-reinforced cross-linked

polyisoprene (SWCNT:CL:PI) composite system. The total energy was measured in units of $k_B T$, set to 1. The parameters used for energy minimization and equilibration were derived from this work and from previous studies, as shown in **Figure 4.4** and **Figure 4.5**, respectively. **Figure 4.4** shows that the total energy of all SWCNT:CL:PI systems is constant at approximately 6.93 DPD unit. The total energy of the PI nanocomposite systems decreased as the SWCNT concentration decreased. The 8% SWCNT:CLPI system had the highest total energy. This was attributed to the nanotube slowing the movement of the PI chains. After energy minimization completed, system equilibration was continued for further 500,000 steps to examine the total energy of the composite system. As can be seen from **Figure 4.5**, the system had reached equilibrium. In addition, the increase in total energy during equilibration was greater than the decrease of that during energy minimization. **Figure 4.6** shows the structure of the 2% SWCNT:CL:PI composite system in the equilibrium state. The inhibition of PI movement in the simulation may affect the mechanical properties of the polymer composite. We therefore studied the structural and dynamical stability of the system.

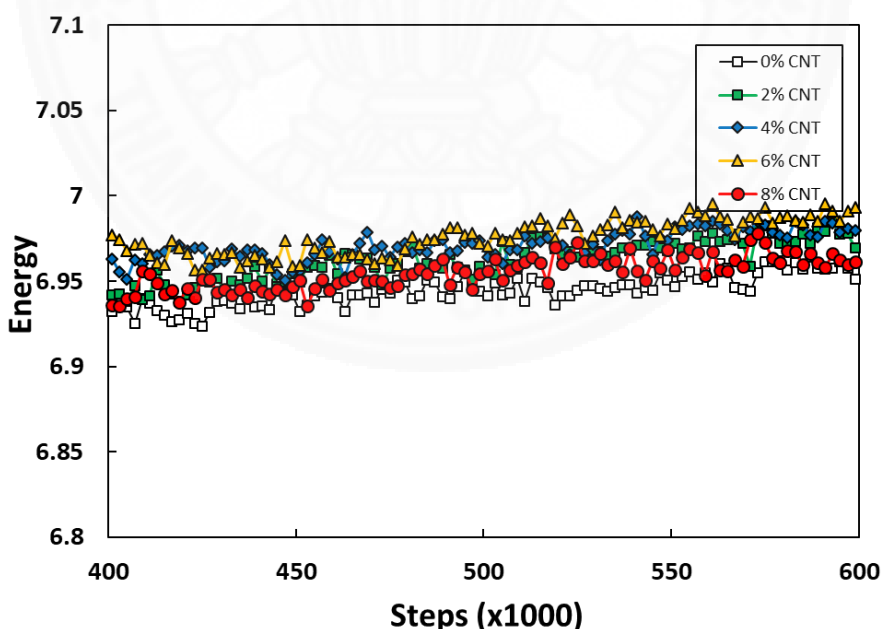


Figure 4.4. Relationship between total energy of SWCNT:CL:PI composite systems and simulation steps during energy minimization calculated by DPD/mSRP model.

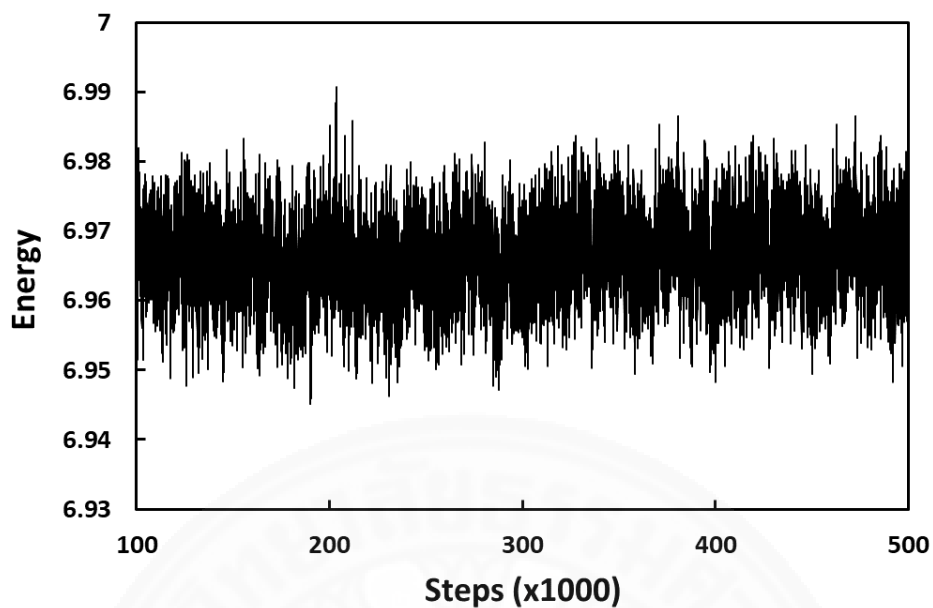


Figure 4.5. Relationship between total energy of 2% SWCNT:CL:PI composite system and simulation steps during equilibration calculated by DPD/mSRP model.

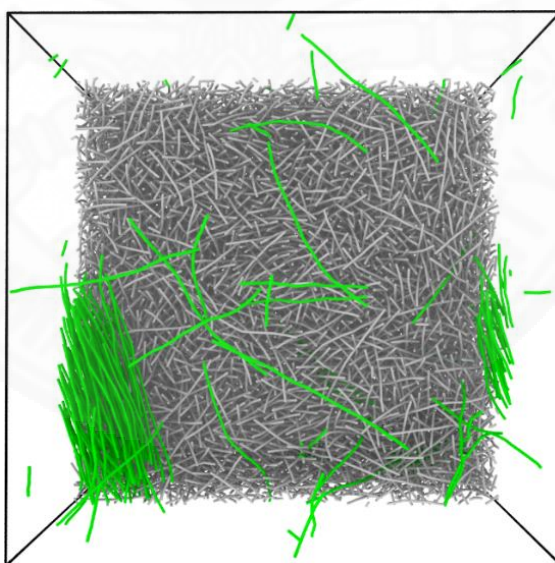


Figure 4.6. Simulated structure of 2% SWCNT:CL:PI composite system in equilibrium state calculated by DPD model. Nanotubes shown in green.

4.2.2 Movement of PI

The mean-square displacement (MSD) was computed to understand the movement of PI and nanotube in non-deformed and deformed states. **Figure 4.7** shows the MSD of the PI at different SWCNT concentrations, in the DPD and DPD/mSRP models. The MSD plots of the two models agreed qualitatively. However, the DPD/mSRP model produced a significantly lower MSD for any given time period. This was attributed to a slow movement of PI. MSD slope decreased as SWCNT concentration decreased. At a 400 τ simulation, the MSD of pure PI system modelled by DPD potential reached $45r_c^2$, while that modelled by DPD/mSRP potential reached only $18r_c^2$. This suggested that polymer chain movement was significantly restricted when the DPD/mSRP model was used, and confirmed that the modified SRP potential affected polymer movement by enforcing PI chain entanglement.

The diffusion of PI, which was related to the change in MSD over time, also had a nonlinear dependency on the SWCNT concentration. Increasing the SWCNT concentration restricted the dynamics, and therefore reduced the diffusion of PI. Chakraborty *et al.* conducted CNT-polycarbonate simulations and attributed the dispersion of CNT aggregates in the polymer matrix to restricted polymer movement.⁽⁸⁵⁾ The change in PI and CNT morphologies from their equilibrium state can be monitored. Karatrantos *et al.* investigated the relationship between the structure of aggregated CNT and enhancement of the mechanical properties.^(100,101) Farhadinia *et al.* attributed an increase in the mechanical modulus to the self-aggregation of CNT.⁽¹⁰²⁾ In addition, at high concentrations, CNTs form multi-layer clusters which disperse in the polymer matrix. This phenomenon affects the elasticity of the polymer by providing a restoring force following the external deformation.⁽¹⁰³⁾

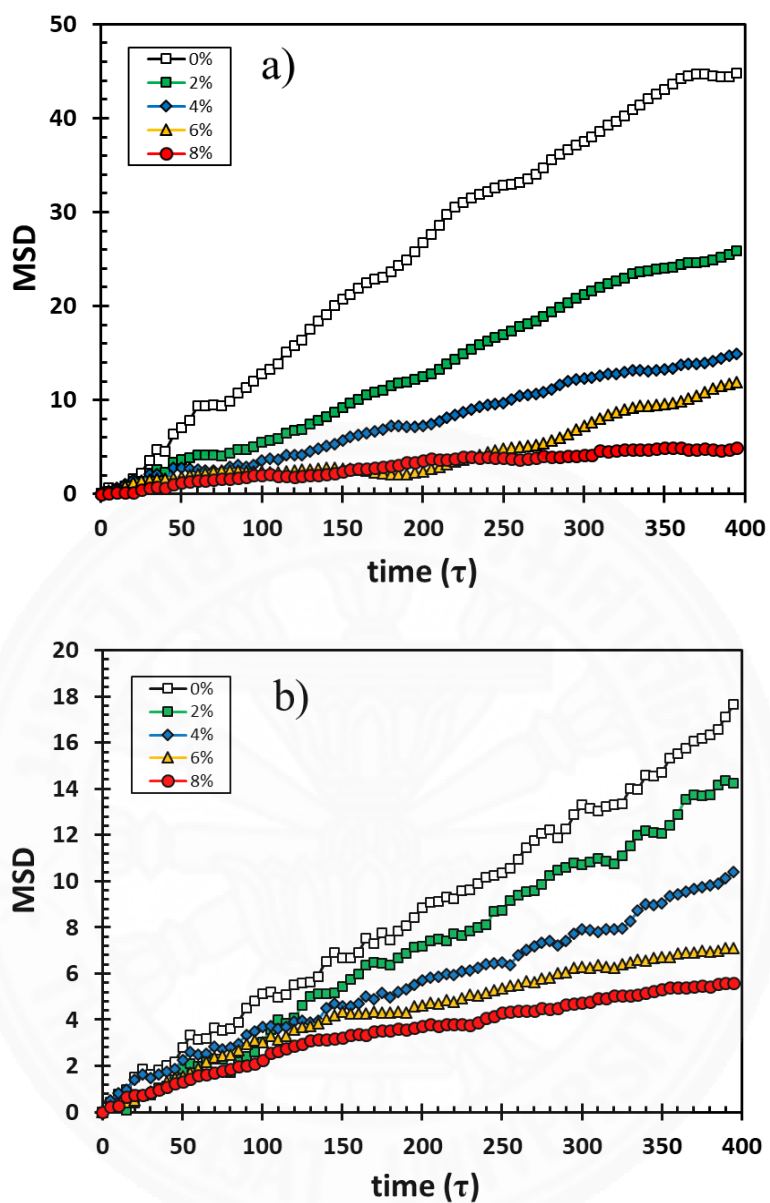


Figure 4.7. MSD of PI during system equilibration at SWCNT concentrations of 0%, 2%, 4%, 6%, and 8%, calculated by (a) DPD and (b) DPD/mSRP models.

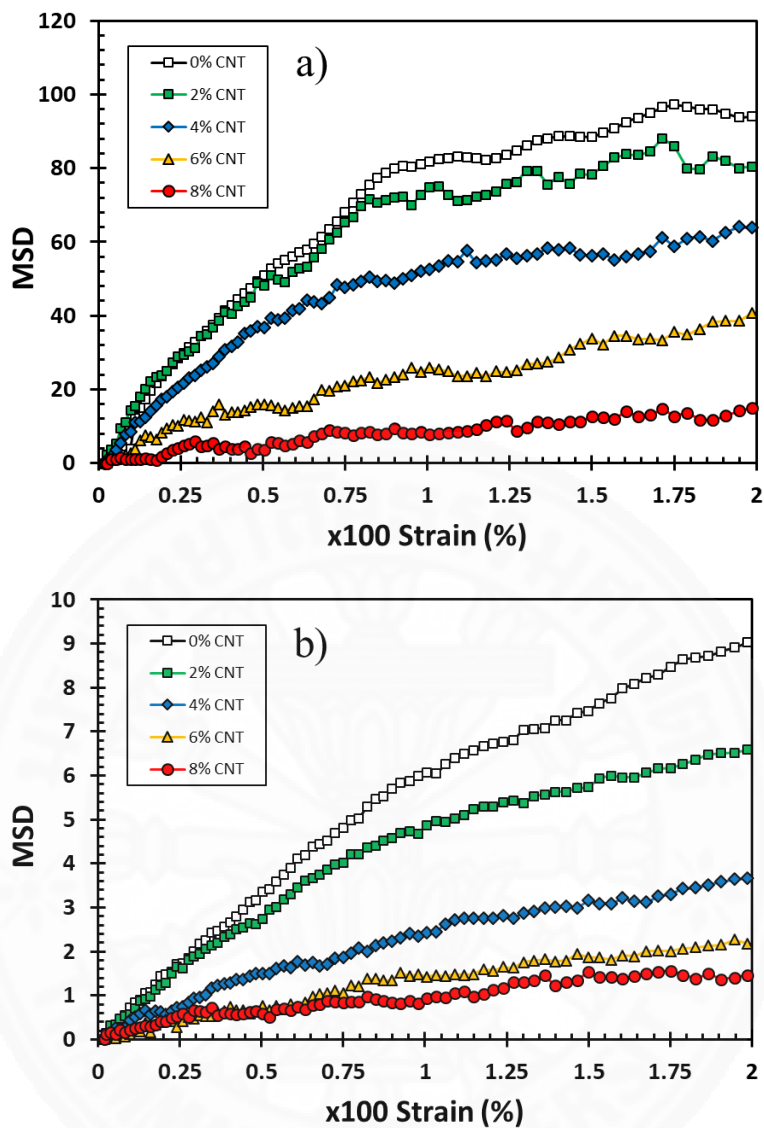


Figure 4.8. MSD of PI under longitudinal deformation at SWCNT concentrations of 0%, 2%, 4%, 6%, and 8%, calculated by (a) DPD and (b) DPD/mSRP models.

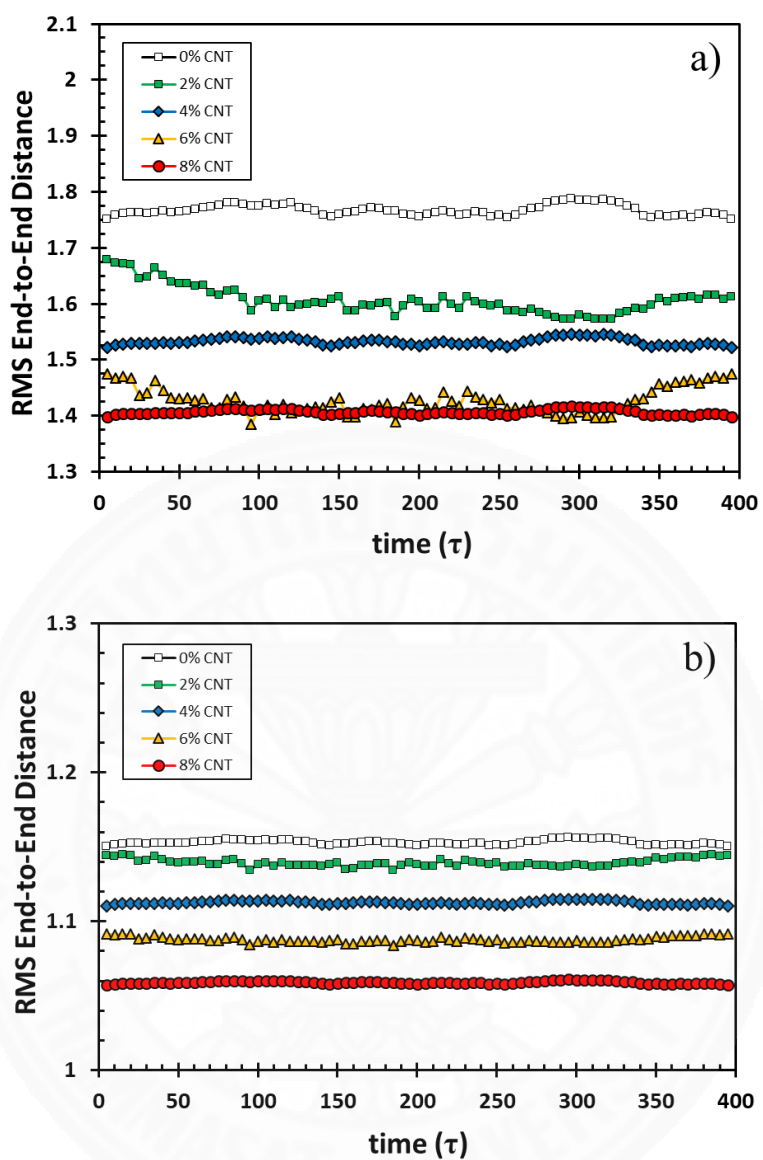


Figure 4.9. RMS end-to-end distance of PI at equilibrium at SWCNT concentrations of 0%, 2%, 4%, 6%, and 8%, calculated by (a) DPD and (b) DPD/mSRP models.

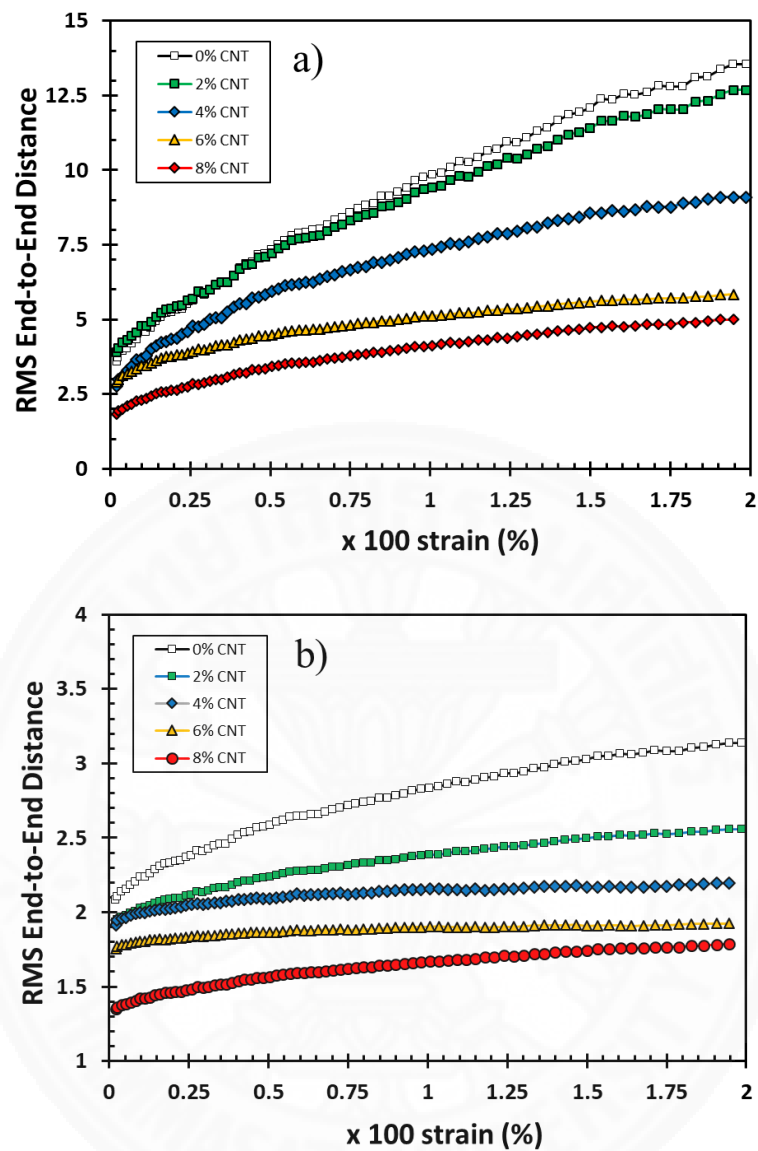


Figure 4.10. RMS end-to-end distance of PI under longitudinal deformation at SWCNT concentrations of 0%, 2%, 4%, 6%, and 8%, calculated by (a) DPD and (b) DPD/mSRP models.

In equilibrated system, PI chains move freely and randomly throughout the simulation. We then applied deformation to the five composite systems shown in **Figure 4.7** until the simulated cell reached 200% strain. Not only MSD plot, but also root mean-squared end-to-end distance $\langle R_{EE} \rangle$ can be used to analyze the structure of PI. The $\langle R_{EE} \rangle$ provides additional dynamical information and elastic properties on the PI behavior.(104) The $\langle R_{EE} \rangle$ plots from the DPD and DPD/mSRP simulations were shown in **Figure 4.9**. As the equilibrating system explores the phase space, the $\langle R_{EE} \rangle$ stays relatively constant. The $\langle R_{EE} \rangle$ from the DPD simulations was greater than that from the DPD/mSRP simulations. This was expected, given the less restricted movement in the DPD simulation. The addition of SWCNT also restricted polymer movement, as evidenced by a decrease in $\langle R_{EE} \rangle$. Because the mechanical properties of a polymer matrix are related to the difficulty of polymer deformation (20), the addition of CNT would be expected to improve the strength of a SWCNT/PI composite.

As shown in **Figure 4.8** and **Figure 4.10**, under deformation the MSD and $\langle R_{EE} \rangle$ values increased in line with strain, in a nonlinear fashion. The change was greatest in the pure polymer. The addition of CNT limited the polymer movement, and therefore the change. For a given strain, the PI of the 8% CNT composite had the lowest MSD and $\langle R_{EE} \rangle$. The DPD model yielded a larger change in both quantities than the DPD/mSRP model, again confirming the role played by mSRP correction in avoiding topology violations.

4.2.3 Movement of SWCNT

The MSD of SWCNT as a function of strain and %CNT is shown in **Figure 4.11**. The MSD increased with the strain, indicating nanotube movement during deformation. Judging from the MSD value, the CNT moved more significantly than the polymer during the deformation. This is partly due to the alignment of the CNT along the deformation and the sliding between the CNTs. Our MSD results agreed with those of Kim and Strachan(105) who reported that CNT moved relatively fast, especially at

low %CNT. The speed of the CNT relative to the matrix decreased when the CNTs were completely enclosed with PI. This reason is in line with **Figure 4.11**, in which the MSD of CNT decreases with increasing %CNT. This indicates entanglement between the CNT and the polymer matrix.

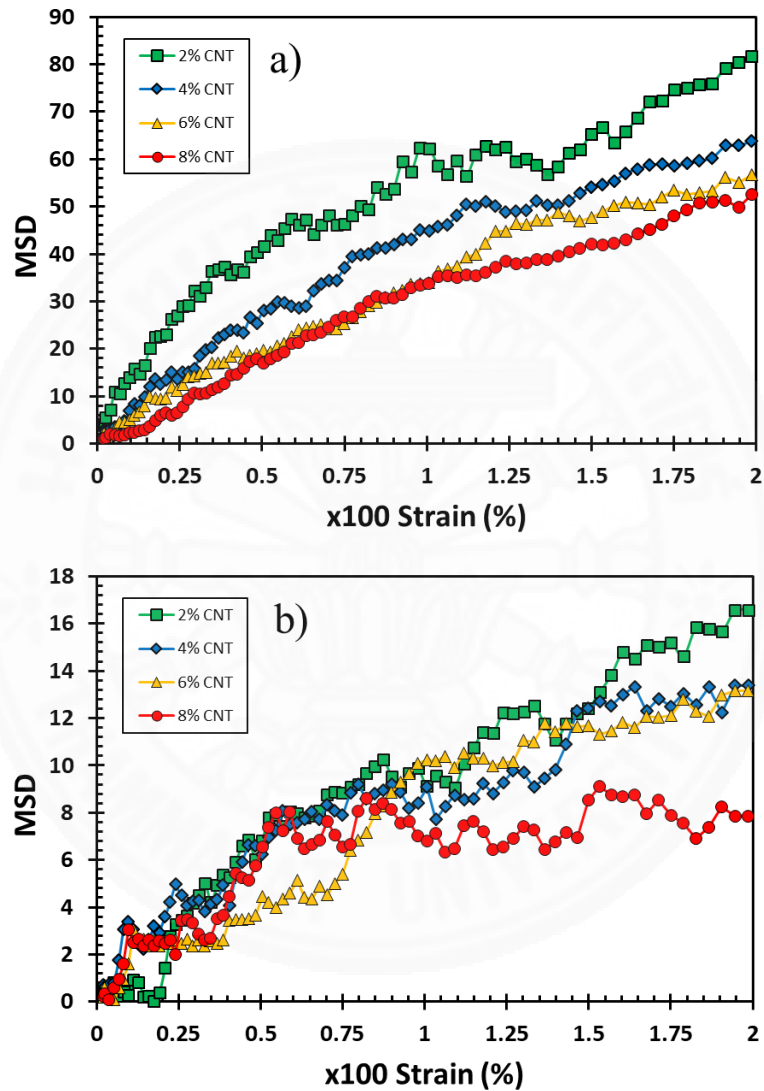


Figure 4.11. MSD of SWCNT during longitudinal deformation at different concentrations of SWCNT: 2%, 4%, 6%, and 8%, calculated by (a) DPD and (b) DPD/mSRP models.

4.2.4 Self-aggregation of CNT

Figure 4.12 shows the snapshot of SWCNT:CL:PI systems in equilibrium at different concentrations: 2%, 4%, 6%, and 8%. We found that the aggregation of nanotubes was in good agreement with those of Chakraborty *et al.*(85) They used atomistic simulation to study the morphology and dynamics of CNT in PC nanocomposite, and observed the bundle formation of CNT at low % mixture.

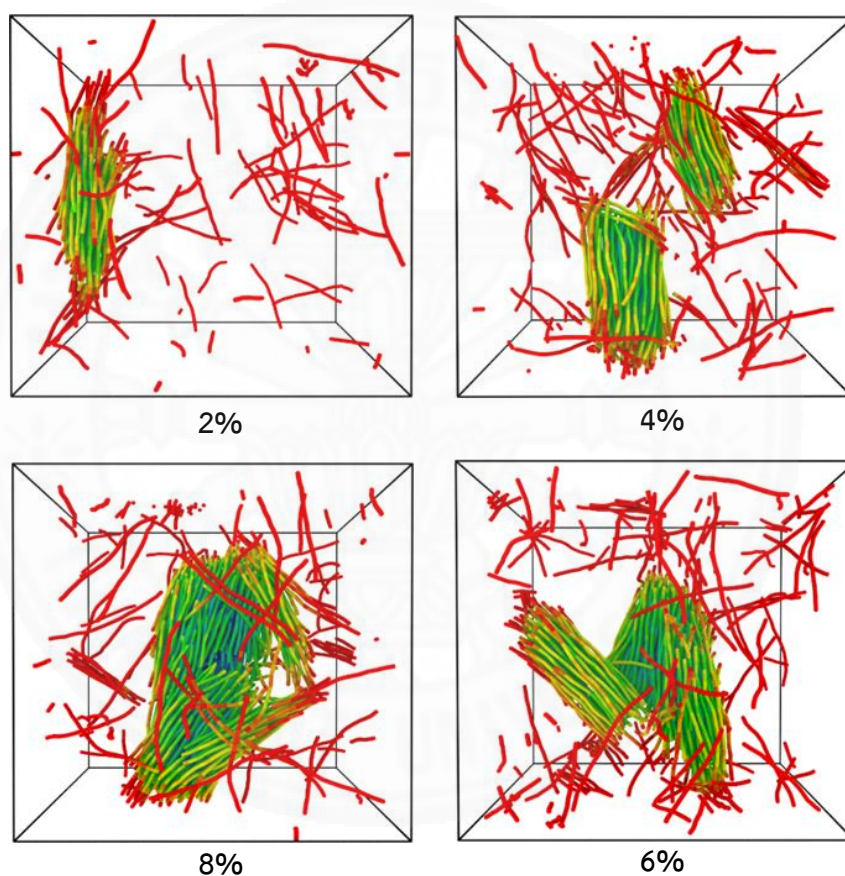


Figure 4.12. Clockwise from top left: aggregated bundle of SWCNTs of 2%, 4%, 6%, and 8% mixtures at equilibrium state calculated by DPD/mSRP model.

We computed the radial distribution function $g(r)$ of SWCNT to determine the minimum distance cutoff (r_c) for defining the aggregation boundary between nanotubes (see **Figure 4.13**). (80) As can be seen from the first peak in $g(r)$ plot, the cutoff distance at $1.25 r_c$ was chosen to quantify the aggregation of

nanotubes. Then the distribution of CNT bundle size was computed. **Figure 4.14** shows the average size distribution of CNT bundle at SWCNT concentrations: 2%, 4%, 6%, and 8%, obtained from any snapshot in equilibrium. We observed that, at low CNT concentration, most SWCNT do not form bundles. 8% SWCNT had the highest in size of bundle. In addition, average size bundle is consistent with the SWCNT concentration, in which nanotube bundles grown larger as the SWCNT concentration increases.

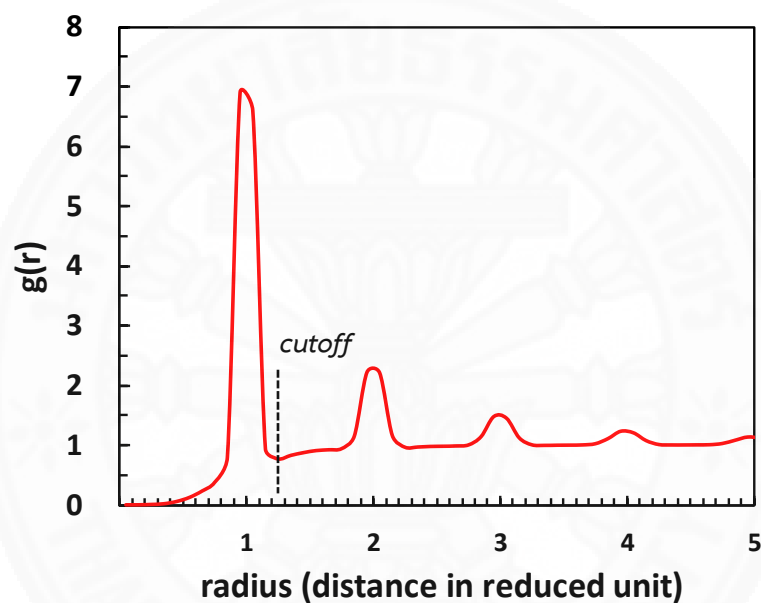


Figure 4.13. Radial distribution function $g(r)$ of CNT for typical SWCNT:CL:PI composite system calculated by DPD/mSRP model. Cutoff for CNT cluster distribution is shown.

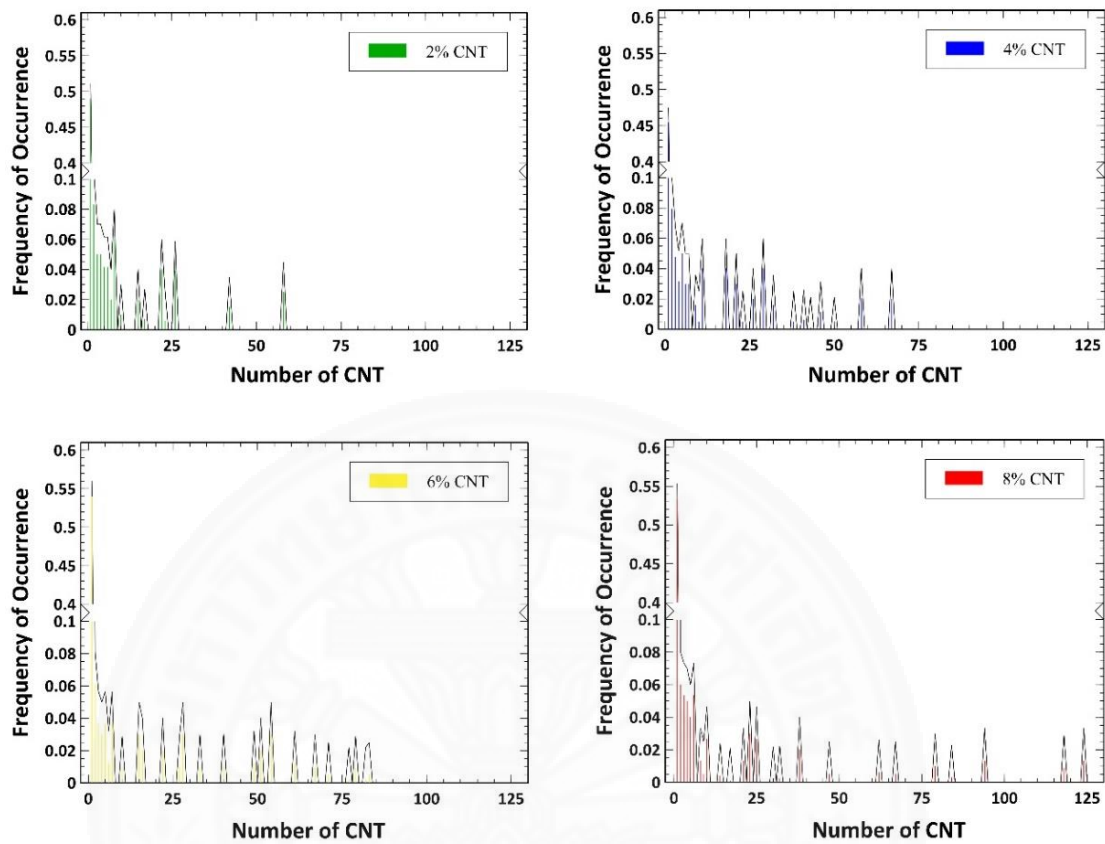


Figure 4.14. Average size distribution of SWCNT bundles at equilibrium state of composite calculated by DPD/mSRP model

Figure 4.15 is a snapshot of CNT bundle in a 2% SWCNT:CL:PI system at 100% and 200% strain. The CNTs bundles during deformation were more dispersed and far apart than that in equilibrium, seen from **Figure 4.12**. The SWCNT bundle system aggregates to form bundles, highlighted in green, and depending on the temperature of the system. Shape and size of the bundle exhibits different SWCNT/PI structures. Furthermore, the CNT bundle tended to align along the deformation direction.

In addition to $\langle R_{EE} \rangle$, the alignment of CNT during deformation (see **Figure 4.15**) was investigated. A directional movement of SWCNT bundle along longitudinal deformation was examined by the orientational order parameter S_{CNT} . **Figure 4.16** shows the relationship of S_{CNT} and strain at different SWCNT

concentrations. It was found that S_{CNT} increased as the simulated box, where contains SWCNT bundle, was direction pulled. At 200% strain, S_{CNT} of all SWCNT concentrations in DPD/mSRP reached approximately 1 regardless of direction of nanotube at initial deformation.

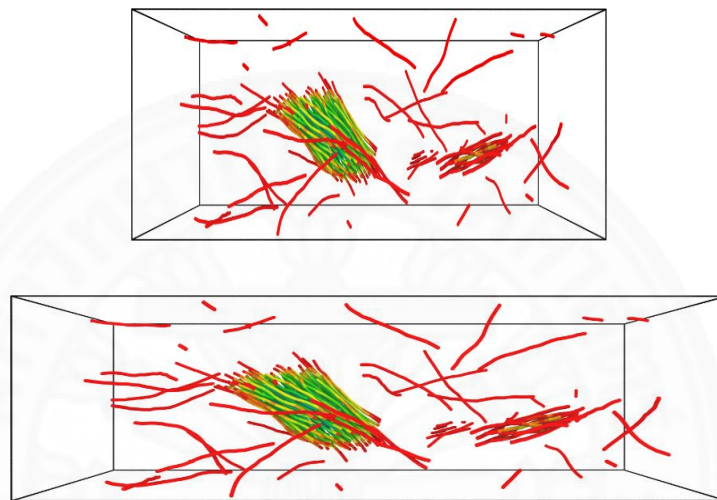


Figure 4.15. Elongation of 2% SWCNT aggregates at (a) 100% and (b) 200% strain calculated by DPD/mSRP model. The identified CNT bundles highlighted in green.

Using several characterization techniques, Xie *et al.* showed that enhancing the alignment and dispersion of SWCNT filler can improve the mechanical properties of polymer.(106) Our simulation showed the same behavior as the CNTs increased the restoring force against deformation. We see the increase of S_{CNT} towards 1.0 as the system became increasingly deformed, hence suggesting the alignment of CNT in the deformation direction. Therefore, the improvement of mechanical strength with the increase of %CNT was attributed to CNT bundle formation and their alignment.(6) However, it is important to note that this behavior is valid only at low CNT concentrations. Uchida and Kumar studied the dispersion and exfoliation of SWCNT in polymer at high CNT concentrations and found that adding overabundant CNTs to composite can reduce the mechanical properties of the polymer.(58)

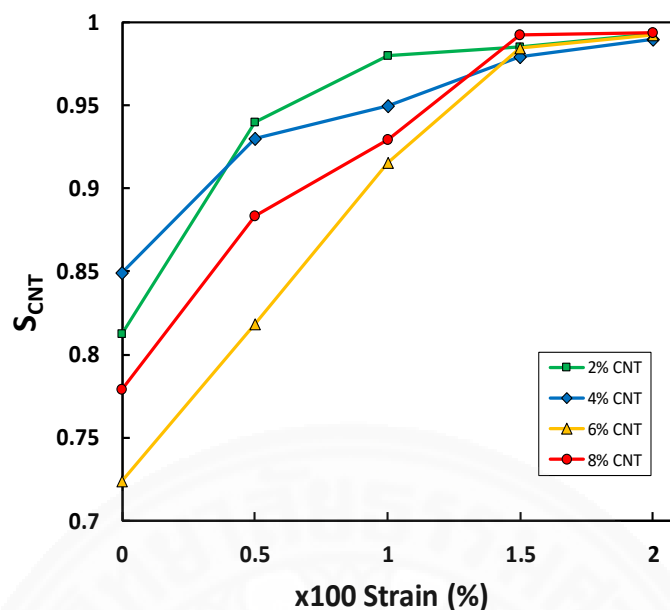


Figure 4.16. The orientational order parameter of CNT (S_{CNT}) with respect to the longitudinal deformation direction during the strain evolution calculated by DPD/mSRP model.

4.3 Mechanical properties

The stress-strain curves of SWCNT:CL:PI composite system were computed on both DPD and DPD/mSRP during an affine uniaxial deformation. The stress at 100% strain was used to determine the 100% Young's modulus, as shown in **Figure 4.17** and **Figure 4.18**. DPD-simulated Modulus is consistent with DPD/mSRP simulation. **Figure 4.17** shows that the stress linearly increased as the applied strain increased from 0% to 200% deformation. The tensile stress at 100% deformation increased from 7 to 14 MPa when the CNT concentrations increased from 0% to 8%. Judging from the stress of the pure CL:PI system and the CNT-reinforced system, the CNT helps strengthen the nanocomposite. However, the DPD-simulated stress-strain curve was weakly depended on the CNT ratio. As in the discussion of the morphology and dynamical properties of PI, the MSD and $\langle R_{EE} \rangle$ described the change of polymer structures when deforming the system. The effect of the increasing CNT concentration

on the stress-strain curve became evident when adopting the DPD/mSRP parameter. The DPD/mSRP-simulated stress-strain curve shown in **Figure 4.18** clearly distinguishes the role of CNT and polymer entanglement in the mechanical properties of the nanocomposites. At 100% deformation, the DPD/mSRP stress of pure CL:PI system was less than that of DPD model. Increasing the CNT from 0% to 8% increased the stress from about 5 MPa to about 23 MPa, reflecting a restricted structural change of polyisoprene. The stress-strain curves from different CNT concentrations hardly overlapped with one another. It appeared that the DPD/mSRP stress was generally less dependent on the strain than that of the DPD.

4.3.1 Young's modulus of SWCNT:CL:PI

As shown in **Figure 4.10**, $\langle R_{EE} \rangle$ of PI during deformation was computed to understand the Young's modulus in DPD and DPD/mSRP simulation. In the case of DPD, PI is easily elongated, while DPD/mSRP-simulated PI was restricted by polymer chain entanglement and was obstructed by SWCNT bundle. We attributed the reason of this to the mSRP self-avoiding model. Our discovery was in good agreement with those of Farhadinia *et al.*, who simulated the CNT-reinforced polymer using MD and reported that the improvement of mechanical strength in PI nanocomposite was increased significantly when adding high SWCNT concentration.(20)

We compared the DPD- and DPD/mSRP-simulated 100% Modulus of sonicated SWCNT/PI composite with the experimental value, as reported in **Table 4.3** and **Figure 4.19**. It was shown that simulated stress at 100% elongation was in good qualitative agreement with that obtained from experiment. The experimental 100% Modulus was obtained from the cross-linked natural rubber composited with the sonicated SWCNT.(7) The 100% Young's modulus of all SWCNT:CL:PI composites simulated by both DPD models were greater than that from experiments. Therefore, the simulated stresses were not in quantitative agreement with the experimental stress. As can be seen from **Figure 4.19**, the DPD and DPD/mSRP stresses increased highly when adding more nanotube concentrations. The former has smaller stress at

high loading, especially 8% SWCNT. In contrast with DPD model, the increasing rate of DPD/mSRP-simulated stress became higher when adding more SWCNT concentrations.

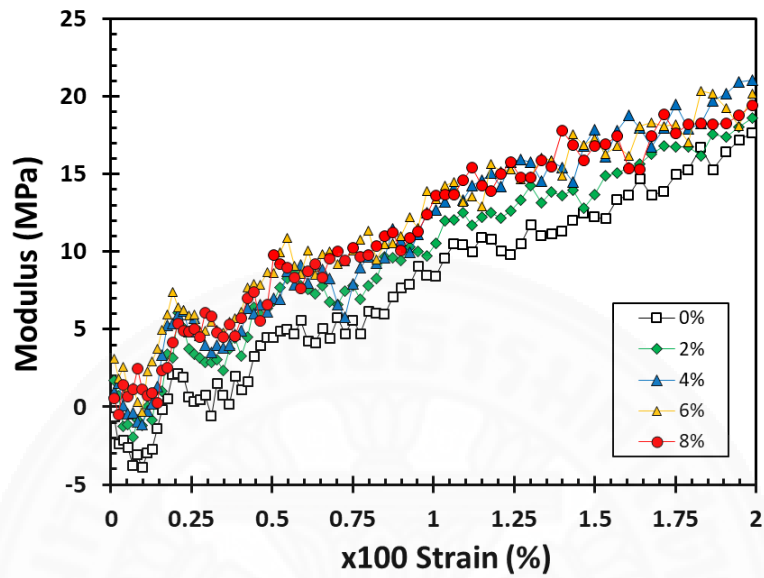


Figure 4.17. Stress-strain curve of SWCNT:CL:PI composite systems at 0-8 % SWCNT calculated by DPD model.

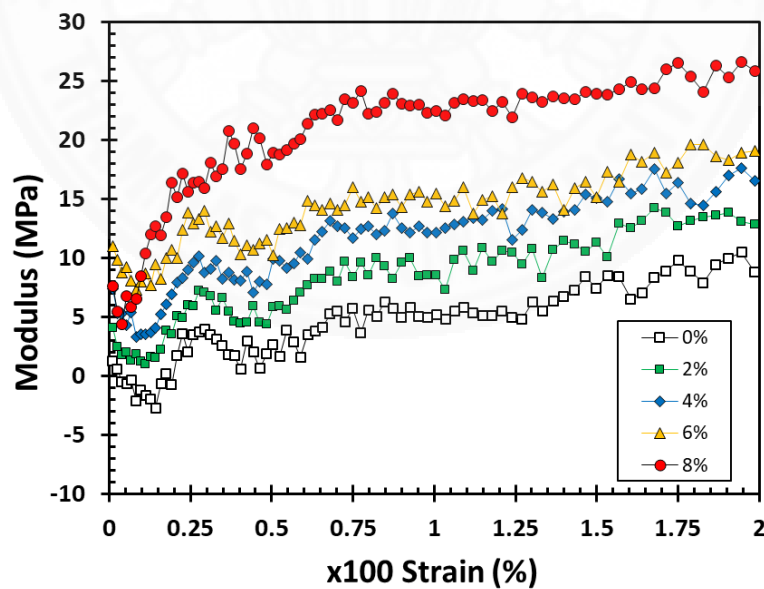


Figure 4.18. Stress-strain curve of SWCNT:CL:PI composite systems at 0-8 % SWCNT calculated by DPD/mSRP model.

Table 4.3. 100% Young's modulus of cross-linked PI composite with CNT by DPD and DPD/mSRP models using the original and modified (marked with an asterisk) PI-PI repulsive parameter (a_{ij}) of 25 and 22.5, respectively.

%CNT	100% Modulus (MPa)				Expt. (7)
	DPD	DPD*	DPD/mSRP	DPD/mSRP*	
0	8.425	5.228	5.167	0.784	0.76 \pm 0.05
2	10.518	8.241	7.548	1.414	1.55 \pm 0.03
4	12.662	9.145	12.182	2.387	2.68 \pm 0.08
6	13.391	12.665	15.421	3.908	3.93 \pm 0.08
8	13.635	13.950	22.467	4.445	4.74 \pm 0.09

4.3.2 DPD reparameterization

As stated in previous section, both DPD- and DPD/mSRP-simulated 100% Young's modulus of PI nanocomposite overestimated the experimental value. The reason for this may be due to the bead-bead repulsive interaction parameter (a_{ij}) between PI beads used in our simulation is overabundant. Previous studies have shown that it is necessary to modify the repulsive interaction parameter to overcome this issue. For example, Trofimov *et al.* modified the repulsive parameter using the MDPD model, which was introduced by Pagonabarraga and Frenkel.(107,108) Padding *et al.* studied the number of polymer chain crossing by using MD simulation and investigated the suitable a_{ij} to improve polymer melt modeling.(28) Another study of Padding *et al.* modified of a_{ij} parameter of PI-PI based on the experimental compressibility of water and equation of state for fluid simulation.(19) In addition, Maiti and McGrother studied the role of increasing a_{ij} on the surface tension of a segregated binary mixture.(89) Moreover, Nikunen *et al.* investigated the dynamical stabilities of a linear homopolymer (109) and observed that the correct polymer dynamics was based on

the proper repulsive interaction parameter. Trofimov *et al.* also suggested that adjusting DPD parameter do not guarantee that the DPD simulation can reproduce the experimental properties. (99) This is due to the nature of the equation of state used in simulation. We therefore reparameterized the DPD parameter to reproduce the Young's modulus by systematically reducing PI-PI repulsive interaction with four values: 25.00, 23.75, 22.50, and 20.00.(25) The computed 100% Modulus of a pure PI system was obtained at different a_{ii} as reported in **Table 4.4**. The decrease of a_{ii} value reduced the 100% Young's modulus. The Young's modulus decreased from 5.167 MPa to 0.764 MPa when a_{ii} of PI-PI was decreased from 25.00 to 22.50 DPD units. This new value was therefore adopted for the quantitative prediction of 100% Young's modulus in SWCNT:CL:PI composites.

Table 4.4. Computed 100% Young's modulus of the pure polyisoprene as a function of reparameterized a_{ii} term for DPD/mSRP simulation.

Entry	a_{ii} of polyisoprene	Computed 100% modulus (Expt. = 0.76 MPa)
1	25.00 ^a	5.167
2	23.75	1.981
3	22.50	0.784
4	20.00	0.334

^aStandard repulsive parameter of polyisoprene used for original DPD and DPD/mSRP simulations.

The 100% Young's modulus of SWCNT:CL:PI composites with different CNT concentrations were recalculated by the DPD/mSRP model with a modified a_{ii} . As can be seen in **Table 4.4**, the 100 % Modulus significantly reduced as PI-PI repulsive interaction decreased. We found that $a_{ii} = 22.50$ produced the 100% Modulus that was in good agreement with experiment value. We therefore used this value in both DPD and DPD/mSRP model to calculate the stress-strain curve of SWCNT:CL:PI composite

system, denoted here as the DPD* and DPD/mSRP* models, respectively. **Figure 4.19** compares the 100% Young's modulus calculated by DPD and DPD/mSRP ($a_{ij} = 25.00$) and that of a modified $a_{ij} = 22.50$, as denoted as DPD* and DPD/mSRP*. We found that the 100% Modulus calculated by latter model is very close to the experimental values of Sae-Oui *et al.*(7) Based on our finding, the DPD and DPD/mSRP models with $a_{ij} = 22.50$ yield the best computed 100% Modulus.

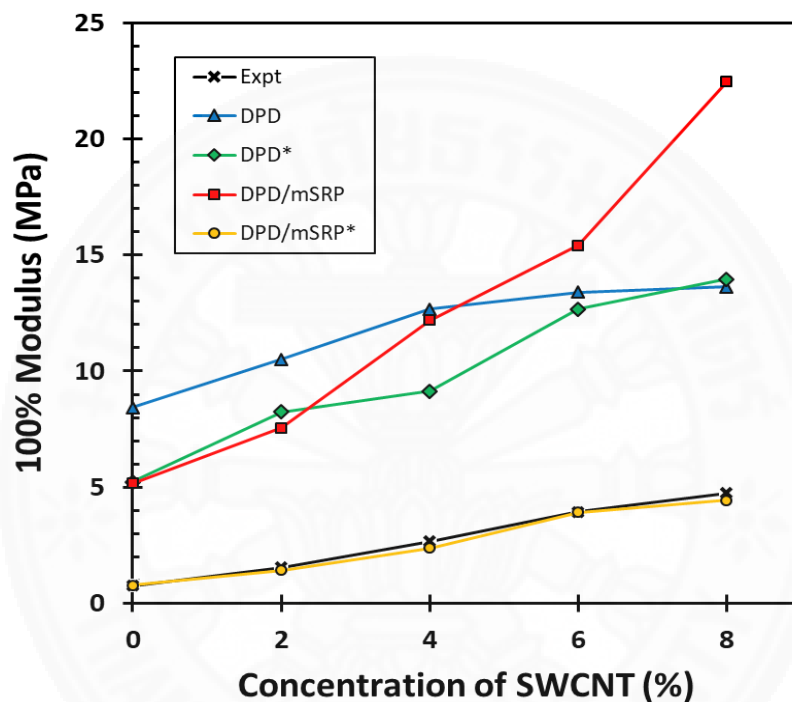


Figure 4.19. 100% Young's modulus as a function of SWCNT concentrations by DPD and DPD/mSRP models using the original and modified (marked here with asterisks) PI-PI repulsive parameter (a_{ij}) of 25.00 and 22.50.

CHAPTER 5

CONCLUSIONS AND RECOMMENDATIONS

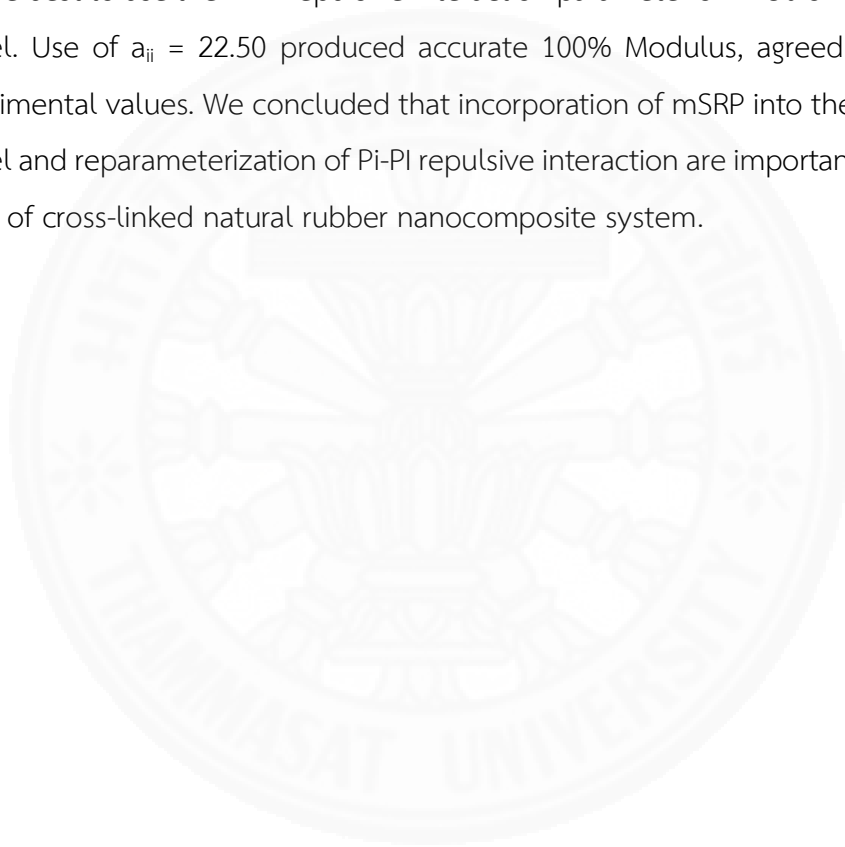
We simulated the mechanical properties of the SWCNT:CL:PI composite system based on the DPD framework. SWCNT loadings were varied with five concentrations: 0%, 2%, 4%, 6%, and 8%. The stress-strain curves were computed to quantify the Young's modulus of all SWCNT:CL:PI systems. In the case of pure PI, the study indicated that polymer chain crossings significantly occur during dynamics simulation, especially deformation. Crossing of PI chains inhibits polymer entanglement, which could lower the mechanical strength, leads polymer to less resistant to external forces. We found that topology violation decreased when particles was moving slow. The use of small time step size is therefore useful for simulating polymeric system. We also found that mechanical properties of PI are dominated by entanglement of polymer.

Because the DPD model could not describe the polymer entanglement correctly, DPD/mSRP repulsive potential was used to enhance PI chain entanglement. Our results showed that the DPD/mSRP model significantly reduces the number of PI chain crossings than the DPD model. With the self-avoiding of PI chain crossing, the qualitative prediction in mechanical properties of PI nanocomposite could be accurately described. The Young's modulus of PI composite improved as the SWCNT concentrations increased.

In addition to PI entanglement, at high SWCNT concentrations, mean squared displacement and root mean-squared end-to-end distance showed that PI was moving slow due to the fact that its movement was obstructed by SWCNT bundle. We found that the self-aggregation of SWCNT took place in equilibrium state. The distribution of SWCNT bundles occurrence was investigated. In PI nanocomposite, a small SWCNT bundle was found at low CNT concentrations, but that became larger at high concentrations. The orientational order parameter was used to monitor the directional change of SWCNT-aggregated bundle during deformation. The SWCNT

bundle in all PI composites aligned along with the directional deformation when increasing strain for both DPD and DPD/mSRP models. Enhancement of mechanical strength of PI composite was also attributed to self-aggregation of SWCNT causing a restricted polymer movement.

To quantitatively predict the mechanical properties of PI nanocomposite, we parameterized the PI-PI repulsive interaction parameter. Based on our investigation, it is the best to use the PI-PI repulsive interaction parameter of 22.50 on the DPD/mSRP model. Use of $a_{ij} = 22.50$ produced accurate 100% Modulus, agreed well with the experimental values. We concluded that incorporation of mSRP into the standard DPD model and reparameterization of Pi-Pi repulsive interaction are important for long-term study of cross-linked natural rubber nanocomposite system.



REFERENCES

1. Al-Hartomy OA, Al-Ghamdi AA, Al-Salamy F, Dishovsky N, Slavcheva D, EL-Tantawy F. Properties of Natural Rubber-Based Composites Containing Fullerene. *International Journal of Polymer Science*. 2012 Nov 29;2012.
2. Jang SM, Li M-C, Lim JH, Cho UR. Study on Properties of Natural Rubber Compound Using Starch as Filler. *Asian Journal of Chemistry*. 2013 Aug;25(9):5221–5.
3. Salleh SZ, Ahmad MZ, Ismail H. Properties of Natural Rubber/Recycled Chloroprene Rubber Blend: Effects of Blend Ratio and Matrix. *Procedia Chemistry*. 2016 Jan 1;19:346–50.
4. Miyagawa H, Misra M, Mohanty AK. Mechanical Properties of Carbon Nanotubes and Their Polymer Nanocomposites. *Journal of Nanoscience and Nanotechnology*. 2005 Oct 1;5(10):1593–615.
5. WenXing B, ChangChun Z, WanZhao C. Simulation of Young's modulus of single-walled carbon nanotubes by molecular dynamics. *Physica B: Condensed Matter*. 2004 Oct;352(1–4):156–63.
6. Tonpheng B, Yu J, Andersson BM, Andersson O. Tensile Strength and Young's Modulus of Polyisoprene/Single-Wall Carbon Nanotube Composites Increased by High Pressure Cross-linking. *Macromolecules*. 2010 Sep 28;43(18):7680–8.
7. Sae-Oui P, Thepsuwan U, Thaptong P, Sirisinha C. Comparison of Reinforcing Efficiency of Carbon Black, Conductive Carbon Black, and Carbon Nanotube in Natural Rubber. *Advances in Polymer Technology*. 2014 Dec;33(4):21422.
8. Bueche F. Mechanical properties of natural and synthetic rubbers. *Journal of Polymer Science*. 1957 Aug;25(110):305–24.
9. PUȘCĂ A, BOBANCU Ș, DUȚĂ A. Mechanical Properties of Rubber - An Overview. 2010;3:107–14.
10. Grokhovskaya TY, Volynskii AL, Bakeyev NF. Mechanical properties of vulcanized natural rubber filled with a linear crystallizing hydrocarbon. *Polymer Science USSR*. 1989 Jan 1;31(7):1612–6.

11. Abd-El Salam F, Abd-El Salam MH, Mostafa MT, Nagy MR, Mohamed MI. Effect of the vulcanizing system on the mechanical properties of butyl rubber/ethylene propylene diene monomer-carbon black blends. *Journal of Applied Polymer Science*. 2003 Nov 7;90(6):1539–44.
12. Yang G, Liao Z, Yang Z, Tang Z, Guo B. Effects of substitution for carbon black with graphene oxide or graphene on the morphology and performance of natural rubber/carbon black composites. *Journal of Applied Polymer Science*. 2015 Apr 15;132(15).
13. Azira AA, Kamal MM, Rusop M. Reinforcement of graphene in natural rubber nanocomposite. In 2016. p. 020003.
14. Zhang T, Kumari L, Du GH, Li WZ, Wang QW, Balani K, et al. Mechanical properties of carbon nanotube–alumina nanocomposites synthesized by chemical vapor deposition and spark plasma sintering. *Composites Part A: Applied Science and Manufacturing*. 2009 Jan;40(1):86–93.
15. Khan F, Ahmad SR, Syed AA. Nanotube composites produced from single-walled carbon nanotubes and polycarbonate. 2007;7(1):344–7.
16. Meier RJ. Applications of Ab-Initio Molecular Dynamics Simulations in Chemistry and Polymer Science. In: *Computational Molecular Dynamics: Challenges, Methods, Ideas*. Springer, Berlin, Heidelberg; 1999. p. 433–41. (Lecture Notes in Computational Science and Engineering).
17. Hernández ER. Molecular Dynamics: from basic techniques to applications (A Molecular Dynamics Primer). *AIP Conference Proceedings*. 2008 Nov 13;1077(1):95–123.
18. Kmiecik S, Gront D, Kolinski M, Wieteska L, Dawid AE, Kolinski A. Coarse-Grained Protein Models and Their Applications. *Chemical Reviews*. 2016 Jul 27;116(14):7898–936.
19. Padding JT, Briels WJ. Time and length scales of polymer melts studied by coarse-grained molecular dynamics simulations. *The Journal of Chemical Physics*. 2002 Jun 24;117(2):925–43.

20. Hagita K, Morita H, Doi M, Takano H. Coarse-Grained Molecular Dynamics Simulation of Filled Polymer Nanocomposites under Uniaxial Elongation. *Macromolecules*. 2016 Mar 8;49(5):1972–83.
21. Moeendarbary E, Ng TY, Zangeneh M. Dissipative particle dynamics: introduction, methodology and complex fluid applications - a review. *International Journal of Applied Mechanics*. 2009;1(04):737–763.
22. Groot RD, Warren PB. Dissipative particle dynamics: Bridging the gap between atomistic and mesoscopic simulation. *The Journal of Chemical Physics*. 1997 Sep 15;107(11):4423–35.
23. Sirk TW, Slizoberg YR, Brennan JK, Lisal M, Andzelm JW. An enhanced entangled polymer model for dissipative particle dynamics. *The Journal of Chemical Physics*. 2012 Apr 7;136(13):134903.
24. Krafnick RC, García AE. Efficient Schmidt number scaling in dissipative particle dynamics. *The Journal of Chemical Physics*. 2015 Dec 28;143(24):243106.
25. Español P, Warren PB. Perspective: Dissipative particle dynamics. *The Journal of Chemical Physics*. 2017 Apr 21;146(15):150901.
26. Bulacu M, Goga N, Zhao W, Rossi G, Monticelli L, Periole X, et al. Improved Angle Potentials for Coarse-Grained Molecular Dynamics Simulations. *Journal of Chemical Theory and Computation*. 2013 Aug 13;9(8):3282–92.
27. Shaffer JS. Effects of chain topology on polymer dynamics: Bulk melts. *The Journal of Chemical Physics*. 1994 Sep;101(5):4205–13.
28. Padding JT, Briels WJ. Uncrossability constraints in mesoscopic polymer melt simulations: Non-Rouse behavior of C120H242. *The Journal of Chemical Physics*. 2001 Aug 8;115(6):2846–59.
29. Goujon F, Malfreyt P, Tildesley DJ. Mesoscopic simulation of entanglements using dissipative particle dynamics: Application to polymer brushes. *The Journal of Chemical Physics*. 2008 Jul 21;129(3):034902.
30. Kumar S, Larson RG. Brownian dynamics simulations of flexible polymers with spring–spring repulsions. *The Journal of Chemical Physics*. 2001 Apr 6;114(15):6937–41.

31. Poier P, Likos CN, Moreno AJ, Blaak R. An Anisotropic Effective Model for the Simulation of Semiflexible Ring Polymers. *Macromolecules*. 2015 Jul 28;48(14):4983–97.
32. Thompson AP, Plimpton SJ, Mattson W. General formulation of pressure and stress tensor for arbitrary many-body interaction potentials under periodic boundary conditions. *The Journal of Chemical Physics*. 2009 Oct 19;131(15):154107.
33. Gao Y, Liu J, Shen J, Zhang L, Guo Z, Cao D. Uniaxial deformation of nanorod filled polymer nanocomposites: a coarse-grained molecular dynamics simulation. *Physical Chemistry Chemical Physics*. 2014 Jun 25;16(30):16039.
34. Chantawansri TL, Sirk TW, Sliozberg YR. Entangled triblock copolymer gel: Morphological and mechanical properties. *The Journal of chemical physics*. 2013;138(2):024908.
35. Wu L, Liao S, Zhang S, Bai X, Hou X. Enhancement of mechanical properties of natural rubber with maleic anhydride grafted liquid polybutadiene functionalized graphene oxide. *Chin J Polym Sci*. 2015 Jul 1;33(7):1058–68.
36. Masa A, Saito H, Sakai T, Kaesaman A, Lopattananon N. Morphological evolution and mechanical property enhancement of natural rubber/polypropylene blend through compatibilization by nanoclay. *Journal of Applied Polymer Science*. 2016 Nov 7;134(10).
37. Al-Saleh MH, Sundararaj U. Review of the mechanical properties of carbon nanofiber/polymer composites. *Composites Part A: Applied Science and Manufacturing*. 2011 Dec;42(12):2126–42.
38. Rodriguez AJ, Guzman ME, Lim C-S, Minaie B. Mechanical properties of carbon nanofiber/fiber-reinforced hierarchical polymer composites manufactured with multiscale-reinforcement fabrics. *Carbon*. 2011 Mar 1;49(3):937–48.
39. Medjo RE. Characterization of Carbon Nanotubes. 2013;171–93.
40. Herrero-Latorre C, Álvarez-Méndez J, Barciela-García J, García-Martín S, Peña-Creciente RM. Characterization of carbon nanotubes and analytical methods for their determination in environmental and biological samples: A review. *Analytica Chimica Acta*. 2015 Jan 1;853:77–94.

41. Belin T, Epron F. Characterization methods of carbon nanotubes: a review. *Materials Science and Engineering: B*. 2005 May 25;119(2):105–18.
42. Misra A, Raney JR, De Nardo L, Craig AE, Daraio C. Synthesis and Characterization of Carbon Nanotube–Polymer Multilayer Structures. *ACS Nano*. 2011 Oct 25;5(10):7713–21.
43. Branca C, Frusteri F, Magazù V, Mangione A. Characterization of Carbon Nanotubes by TEM and Infrared Spectroscopy. *J Phys Chem B*. 2004 Mar 1;108(11):3469–73.
44. Choi J-H, Jegal J, Kim W-N. Fabrication and characterization of multi-walled carbon nanotubes/polymer blend membranes. *Journal of Membrane Science*. 2006 Nov 1;284(1):406–15.
45. Gulotty R, Castellino M, Jagdale P, Tagliaferro A, Balandin AA. Effects of Functionalization on Thermal Properties of Single-Wall and Multi-Wall Carbon Nanotube–Polymer Nanocomposites. *ACS Nano*. 2013 Jun 25;7(6):5114–21.
46. Natsuki T, Hayashi T, Endo M. Mechanical properties of single- and double-walled carbon nanotubes under hydrostatic pressure. *Applied Physics A*. 2006 Feb 3;83(1):13–7.
47. Wei X, Chen Q, Peng L-M, Cui R, Li Y. Tensile Loading of Double-Walled and Triple-Walled Carbon Nanotubes and their Mechanical Properties. *J Phys Chem C*. 2009 Oct 1;113(39):17002–5.
48. Lalwani G, Henslee AM, Farshid B, Lin L, Kasper FK, Qin Y-X, et al. Two-Dimensional Nanostructure-Reinforced Biodegradable Polymeric Nanocomposites for Bone Tissue Engineering. *Biomacromolecules*. 2013 Mar 11;14(3):900–9.
49. Tarawneh MA, Ahmad SH, Yahya SY, Rasid R, Noum SYE. Mechanical properties of thermoplastic natural rubber reinforced with multi-walled carbon nanotubes. *Journal of Reinforced Plastics and Composites*. 2011 Feb 1;30(4):363–8.
50. Gao J, He Y, Gong X, Xu J. The role of carbon nanotubes in promoting the properties of carbon black-filled natural rubber/butadiene rubber composites. *Results in Physics*. 2017 Jan 1;7:4352–8.

51. Shvartzman-Cohen R, Florent M, Goldfarb D, Szleifer I, Yerushalmi-Rozen R. Aggregation and Self-Assembly of Amphiphilic Block Copolymers in Aqueous Dispersions of Carbon Nanotubes. *Langmuir*. 2008 May 1;24(9):4625–32.
52. Ahir SV, Huang YY, Terentjev EM. Polymers with aligned carbon nanotubes: Active composite materials. *Polymer*. 2008 Aug;49(18):3841–54.
53. Zhao Y, Byshkin M, Cong Y, Kawakatsu T, Guadagno L, Nicola AD, et al. Self-assembly of carbon nanotubes in polymer melts: simulation of structural and electrical behaviour by hybrid particle-field molecular dynamics. *Nanoscale*. 2016 Aug 25;8(34):15538–52.
54. Byrne MT, Gun'ko YK. Recent Advances in Research on Carbon Nanotube–Polymer Composites. *Advanced Materials*. 2010 Apr 18;22(15):1672–88.
55. Vigolo B, Hérold C. Processing Carbon Nanotubes. *Carbon Nanotubes - Synthesis, Characterization, Applications*. 2011;
56. Sui G, Zhong WH, Yang XP, Yu YH, Zhao SH. Preparation and properties of natural rubber composites reinforced with pretreated carbon nanotubes. *Polymers for Advanced Technologies*. 2008 Nov 1;19(11):1543–9.
57. Azam MA, Talib E, Mohamad N, Kasim MS, Rashid MWA. Mechanical and Thermal Properties of Single-Walled Carbon Nanotube Filled Epoxidized Natural Rubber Nanocomposite.
58. Uchida T, Kumar S. Single wall carbon nanotube dispersion and exfoliation in polymers. *Journal of Applied Polymer Science*. 2005 Nov 5;98(3):985–9.
59. Nah C, Lim JY, Cho BH, Hong CK, Gent AN. Reinforcing rubber with carbon nanotubes. *Journal of Applied Polymer Science*. 2010 Jun 3;1574–81.
60. Boonbumrung A, Sae-oui P, Sirisinha C. Reinforcement of Multiwalled Carbon Nanotube in Nitrile Rubber: In Comparison with Carbon Black, Conductive Carbon Black, and Precipitated Silica. *Journal of Nanomaterials*. 2016:1–8.
61. Gorga RE, Lau KKS, Gleason KK, Cohen RE. The importance of interfacial design at the carbon nanotube/polymer composite interface. *Journal of Applied Polymer Science*. 2006 Oct 15;102(2):1413–8.

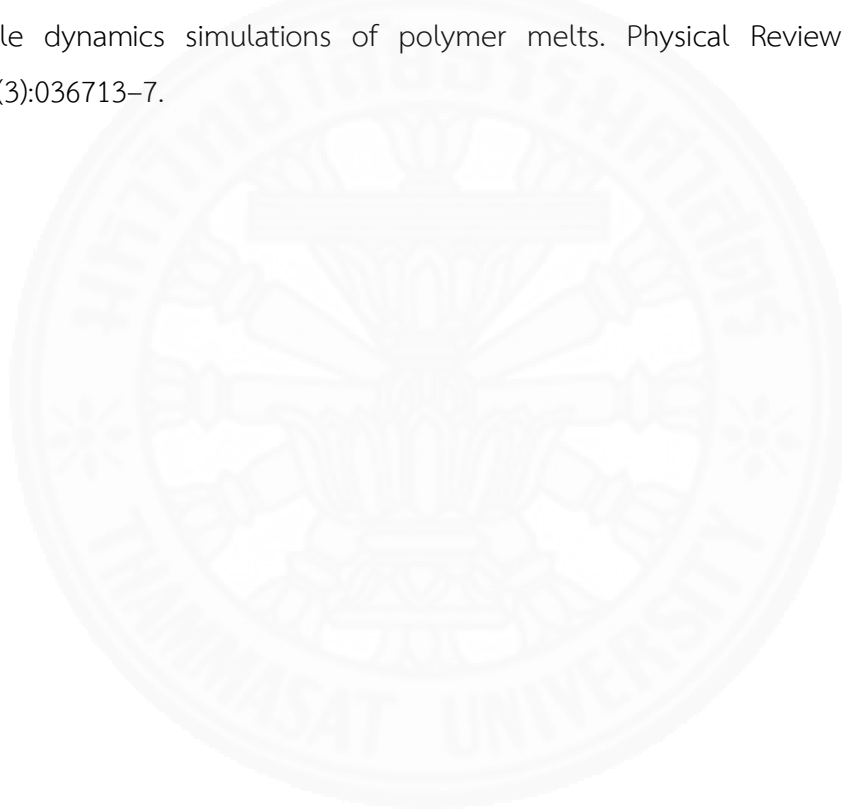
62. Zhu J., Peng H., Rodriguez-Macias F., Margrave J. L., Khabashesku V. N., Imam A. M., et al. Reinforcing Epoxy Polymer Composites Through Covalent Integration of Functionalized Nanotubes. *Advanced Functional Materials*. 2004 Jul 22;14(7):643–8.
63. Gao J, Itkis ME, Yu A, Bekyarova E, Zhao B, Haddon RC. Continuous Spinning of a Single-Walled Carbon Nanotube–Nylon Composite Fiber. *J Am Chem Soc*. 2005 Mar 1;127(11):3847–54.
64. Liu L., Barber A. H., Nuriel S., Wagner H. D. Mechanical Properties of Functionalized Single-Walled Carbon-Nanotube/Poly(vinyl alcohol) Nanocomposites. *Advanced Functional Materials*. 2005 May 27;15(6):975–80.
65. Sun L, Warren GL, O'Reilly JY, Everett WN, Lee SM, Davis D, et al. Mechanical properties of surface-functionalized SWCNT/epoxy composites. *Carbon*. 2008 Feb 1;46(2):320–8.
66. Byrne MT, McNamee WP, Gun'ko YK. Chemical functionalization of carbon nanotubes for the mechanical reinforcement of polystyrene composites. *Nanotechnology*. 2008;19(41):415707.
67. Ruoff RS, Qian D, Liu WK. Mechanical properties of carbon nanotubes: theoretical predictions and experimental measurements. *Comptes Rendus Physique*. 2003 Nov;4(9):993–1008.
68. Arash B, Wang Q, Varadan VK. Mechanical properties of carbon nanotube/polymer composites. *Scientific Reports*. 2014 Oct 1;4:6479.
69. Rafiee R, Rabczuk T, Pourazizi R, Zhao J, Zhang Y. Challenges of the Modeling Methods for Investigating the Interaction between the CNT and the Surrounding Polymer. *Advances in Materials Science and Engineering*. 2013;2013:1–10.
70. Cornwell CF, Wille LT. Elastic properties of single-walled carbon nanotubes in compression. *Solid State Communications*. 1997 Feb 1;101(8):555–8.
71. Frankland S. The stress–strain behavior of polymer–nanotube composites from molecular dynamics simulation. *Composites Science and Technology*. 2003 Aug;63(11):1655–61.

72. Mokashi VV, Qian D, Liu Y. A study on the tensile response and fracture in carbon nanotube-based composites using molecular mechanics. *Composites Science and Technology*. 2007 Mar 1;67(3):530–40.
73. Yang J, Zhang X, Gao P, Gong X, Wang G. Molecular dynamics and dissipative particle dynamics simulations of the miscibility and mechanical properties of GAP/DIANP blending systems. *RSC Adv*. 2014 Sep 8;4(79):41934–41.
74. Frenkel D, Smit B. *Understanding Molecular Simulation - 2nd Edition*. 2001.
75. Allen MP, Tildesley DJ. *Computer Simulation of Liquids*. Reprint edition. Oxford: Clarendon Press; 1989. 408 p.
76. Nieminen RM. From atomistic simulation towards multiscale modelling of materials. *Journal of Physics Condensed Matter*. 2002;14(11):2859–76.
77. Keaveny EE, Pivkin IV, Maxey M, Em Karniadakis G. A comparative study between dissipative particle dynamics and molecular dynamics for simple- and complex-geometry flows. *The Journal of Chemical Physics*. 2005;123(10):104107.
78. Wang Y-C, Lee W-J, Ju S-P. Modeling of the polyethylene and poly(L-lactide) triblock copolymer: A dissipative particle dynamics study. *The Journal of Chemical Physics*. 2009 Sep 22;131(12):124901.
79. Gai J-G, Li H-L, Schrauwen C, Hu G-H. Dissipative particle dynamics study on the phase morphologies of the ultrahigh molecular weight polyethylene/polypropylene/poly(ethylene glycol) blends. *Polymer*. 2009 Jan;50(1):336–46.
80. Wang Y-C, Ju S-P, Cheng H-Z, Lu J-M, Wang H-H. Modeling of Polyethylene and Functionalized CNT Composites: A Dissipative Particle Dynamics Study. *The Journal of Physical Chemistry C*. 2010 Mar 4;114(8):3376–84.
81. Pivkin IV, Caswell B, Karniadakis GE, Lipkowitz K. Dissipative particle dynamics. *Reviews in computational chemistry*. 2011;27:85–110.
82. Tomasini MD, Silvina Tomassone M. Dissipative particle dynamics simulation of poly(ethylene oxide)–poly(ethyl ethylene) block copolymer properties for enhancement of cell membrane rupture under stress. *Chemical Engineering Science*. 2012 Mar;71:400–8.

83. Rodgers B, editor. Rubber Compounding: Chemistry and Applications, Second Edition. 2 edition. CRC Press; 2015. 624 p.
84. Ketkaew R, Tantirungrotechai Y. Dissipative Particle Dynamics Study of SWCNT Reinforced Natural Rubber Composite System: An Important Role of Self-Avoiding Model on Mechanical Properties. *Macromolecular Theory and Simulations*. 2018 Feb 12;1700093.
85. Chakraborty S, Choudhury CK, Roy S. Morphology and Dynamics of Carbon Nanotube in Polycarbonate Carbon Nanotube Composite from Dissipative Particle Dynamics Simulation. *Macromolecules*. 2013 May 14;46(9):3631–8.
86. Liba O, Kauzlaric D, Abrams ZR, Hanein Y, Greiner A, Korvink JG. A dissipative particle dynamics model of carbon nanotubes. *Molecular Simulation*. 2008 Jul;34(8):737–48.
87. Zhou B, Luo W, Yang J, Duan X, Wen Y, Zhou H, et al. Simulation of dispersion and alignment of carbon nanotubes in polymer flow using dissipative particle dynamics. *Computational Materials Science*. 2017 Jan;126:35–42.
88. Chakraborty S, Roy S. Structural, Dynamical, and Thermodynamical Properties of Carbon Nanotube Polycarbonate Composites: A Molecular Dynamics Study. *The Journal of Physical Chemistry B*. 2012 Mar 15;116(10):3083–91.
89. Maiti A, McGrother S. Bead–bead interaction parameters in dissipative particle dynamics: Relation to bead-size, solubility parameter, and surface tension. *The Journal of Chemical Physics*. 2004 Jan 15;120(3):1594–601.
90. Li Y, Kröger M, Liu WK. Primitive chain network study on uncrosslinked and crosslinked cis-polyisoprene polymers. *Polymer*. 2011 Nov;52(25):5867–78.
91. Martínez L, Andrade R, Birgin EG, Martínez JM. PACKMOL: A package for building initial configurations for molecular dynamics simulations. *Journal of Computational Chemistry*. 2009 Oct;30(13):2157–64.
92. Jewett AI, Zhuang Z, Shea J-E. Moltemplate a Coarse-Grained Model Assembly Tool. *Biophysical Journal*. 2013 Jan 29;104(2):169a.
93. Plimpton S. Fast Parallel Algorithms for Short-Range Molecular Dynamics. *Journal of Computational Physics*. 1995 Mar 1;117(1):1–19.

94. Luo C, Sommer J-U. Coding coarse grained polymer model for LAMMPS and its application to polymer crystallization. *Computer Physics Communications*. 2009 Aug;180(8):1382–91.
95. Evans DJ, Holian BL. The Nose–Hoover thermostat. *The Journal of Chemical Physics*. 1985 Oct 15;83(8):4069–74.
96. Coveney PV, Wan S. On the calculation of equilibrium thermodynamic properties from molecular dynamics. *Physical Chemistry Chemical Physics*. 2016;18(44):30236–40.
97. Humphrey W, Dalke A, Schulten K. VMD: Visual molecular dynamics. *Journal of Molecular Graphics*. 1996 Feb 1;14(1):33–8.
98. Stukowski A. Visualization and analysis of atomistic simulation data with OVITO—the Open Visualization Tool. *Modelling and Simulation in Materials Science and Engineering*. 2010 Jan 1;18(1):015012.
99. Trofimov SY, Nies ELF, Michels MAJ. Thermodynamic consistency in dissipative particle dynamics simulations of strongly nonideal liquids and liquid mixtures. *The Journal of Chemical Physics*. 2002 Nov 22;117(20):9383–94.
100. Karatrantos A, Composto RJ, Winey KI, Clarke N. Structure and Conformations of Polymer/SWCNT Nanocomposites. *Macromolecules*. 2011 Dec 27;44(24):9830–8.
101. Karatrantos A, Composto RJ, Winey KI, Kröger M, Clarke N. Entanglements and Dynamics of Polymer Melts near a SWCNT. *Macromolecules*. 2012 Sep 11;45(17):7274–81.
102. Farhadinia M, Arab B, Jam JE. Mechanical Properties of CNT-Reinforced Polymer Nano-composites: A Molecular Dynamics Study. *Mechanics of Advanced Composite Structures*. 2016;3(2):113–121.
103. Kawakatsu T. *Statistical Physics of Polymers: An Introduction*. Berlin Heidelberg: Springer-Verlag; 2004. (Advanced Texts in Physics).
104. Lu T, Chen T, Liang H. Elastic Behavior of Polymer Chains. *Chinese Journal of Chemical Physics*. 2008 Oct 1;21(5):463–8.
105. Kim YJ, Strachan A. CNT-reinforced polymer nanocomposite by molecular dynamics simulations. 2014.

106. Xie X, Mai Y, Zhou X. Dispersion and alignment of carbon nanotubes in polymer matrix: A review. *Materials Science and Engineering: R: Reports*. 2005 May 19;49(4):89–112.
107. Pagonabarraga I, Frenkel D. Non-Ideal DPD Fluids. *Molecular Simulation*. 2000 Aug;25(3–4):167–75.
108. Pagonabarraga I, Frenkel D. Dissipative particle dynamics for interacting systems. *The Journal of Chemical Physics*. 2001 Sep 15;115(11):5015–26.
109. Nikunen P, Vattulainen I, Karttunen M. Reptational dynamics in dissipative particle dynamics simulations of polymer melts. *Physical Review E*. 2007 Mar 30;75(3):036713–7.





APPENDIX A

ANOMALOUS DIFFUSION

MSD plots of PI as a function of time (t) during deformation are non-linear regime, which the PI undergoes anomalous sub-diffusion. We performed non-linear regression and a curve fitting method to estimate the sub-diffusion coefficient (A) measured in the DPD unit and sub-diffusion parameter alpha (α) which are defined by Equation 21.

$$\text{MSD} = A(t)^\alpha \quad 21$$

Table A1. Computed sub-diffusion coefficient (A) and sub-diffusion parameter alpha (α) of PI anomalous diffusion at different concentration of CNT for DPD/mSRP model.

CNT concentrations (%)	A	α
0	1.261	0.9148
2	1.279	0.7006
4	2.705	0.5877
6	3.278	0.5444
8	4.055	0.4259

BIOGRAPHY

Name	Rangsiman Ketkaew
Date of Birth	September 25, 1993
Educational Attainment	2012 - 2016: Degree of Bachelor of Science in Chemistry, Thammasat University 2016 – 2018: Degree of Master of science in Physical Chemistry, Thammasat University
Work Position	Graduate student
Publications	1. Ketkaew, R.; Tantirungrotechai, Y. <i>Macromolecular Theory and Simulations</i> 2018 , 1700093 (1-10). 2. Bunchuay, T.; Ketkaew, R.; Chotmongkolsap, P.; Chutimasakul, T.; Kanarat, J.; Tantirungrotechai, Y.; Tantirungrotechai, J. <i>Catalysis Science & Technology</i> . 2017 , 7, 6069–6079.
Work Experiences	1. NCTU Elite program 2018 – Intern at Computational Chemistry Unit, National Chiao Tung University, Taiwan 2. NCTU Elite program 2015 – Intern at Computational Chemistry Unit, National Chiao Tung University, Taiwan 3. Summer internship at Computational Chemistry Research Unit, Thammasat university, Thailand